

SPACE TELESCOPE IMAGING SPECTROGRAPH SURVEY OF FAR-ULTRAVIOLET CORONAL FORBIDDEN LINES IN LATE-TYPE STARS

THOMAS R. AYRES, ALEXANDER BROWN, GRAHAM M. HARPER, AND RACHEL A. OSTEN
Center for Astrophysics and Space Astronomy, 389 UCB, University of Colorado, Boulder, CO 80309-0389;
ayres@casa.colorado.edu, ab@casa.colorado.edu, gmh@casa.colorado.edu, raosten@casa.colorado.edu

AND

JEFFREY L. LINSKY, BRIAN E. WOOD, AND SETH REDFIELD
JILA, 440 UCB, University of Colorado, Boulder, CO 80309-0440;
jlinsky@jila.colorado.edu, woodb@casa.colorado.edu, sredfiel@casa.colorado.edu

Received 2002 April 11; accepted 2002 October 4

ABSTRACT

We describe an extensive search with the Space Telescope Imaging Spectrograph (STIS) for ultraviolet coronal ($T > 10^6$ K) forbidden lines in a sample of 29 F–M dwarfs, giants, and supergiants. Measuring coronal lines in the 1150–1700 Å band with STIS has important advantages of superior velocity resolution and an absolute wavelength calibration compared with using the *Chandra* or *XMM-Newton* grating spectrometers to observe permitted transitions of the same ion stages in the kilovolt X-ray region. Fe XII $\lambda\lambda 1242, 1349$ ($T \sim 2 \times 10^6$ K) and Fe XXI $\lambda 1354$ (10^7 K) are well known from solar studies and have been reported in previous stellar work. A search for other coronal forbidden lines in the 1200–1600 Å region was largely negative. The few candidate identifications (e.g., Ar XIII $\lambda 1330$ and Ca XV $\lambda 1375$) are too faint to be diagnostically useful. We add new dwarfs to the list of Fe XII detections, including the nearby solar twin α Cen A (G2 V). Clear detections of Fe XXI were obtained in dMe stars, active giants, a short-period RS CVn binary, and possibly in active solar-type dwarfs. We developed a semiempirical method for removing the C I blend that partially affects the Fe XXI $\lambda 1354$ profile. As discussed recently by Johnson et al., Capella (α Aur; G8 III+G1 III) displays clear Fe XXI variability between Goddard High-Resolution Spectrograph (GHRS) and STIS observations 4 yr apart, which is apparently due to a substantial decline in the contribution from the G8 primary. We present an alternative model of the GHRS and STIS era profiles using information in the two sets of line shapes jointly, as well as knowledge of the behavior of Fe XXI profiles of other late-G “clump” giants similar to Capella G8. The full survey sample also provides a context for the apparent variability: the Fe XXI flux of the G8 star in the GHRS spectrum is nearly identical (in $L_{\text{Fe XXI}}/L_{\text{bol}}$) to other clump giants of similar L_X/L_{bol} , but it had dropped at least a factor of 6 in the STIS measurement. The He II $\lambda 1640$ B α feature—which is thought to be responsive to coronal irradiation—also showed significant changes between the GHRS and STIS epochs, but the decrease in the G8 star was much smaller than Fe XXI. The Fe XII flux displays a correlation with the *ROSAT* 0.2–2 keV X-ray flux that can be described by an $\alpha = 0.5$ power law. Fe XXI exhibits a steeper, perhaps linear ($\alpha = 1$), correlation with the *ROSAT* flux down to an activity level of $L_X/L_{\text{bol}} \sim 10^{-5}$, below which detections of the coronal forbidden line are rare. There is no evidence of large, systematic Doppler shifts in either Fe XII $\lambda 1242$ or Fe XXI $\lambda 1354$. This suggests that the emissions arise dominantly in confined structures, analogous to magnetic loops on the Sun, rather than, say, in a hot wind. The Fe XII and Fe XXI line widths generally are close to thermal (FWHM ~ 40 – 90 km s $^{-1}$ at $T \sim 10^{6.2}$ – $10^{7.0}$ K), except for the Hertzsprung-gap giants 31 Comae (G0 III) and Capella G1 and the K1 subgiant primary of HR 1099, all of which show evidence for excess broadening in Fe XXI (Fe XII is obscured in these objects by broad N V $\lambda 1242$ features). If the excess broadening is rotational, it implies that the hot coronae of “X-ray-deficient” 31 Com and Capella G1 are highly extended, contrary to the compact structures suggested by recent density estimates in a number of active coronal sources.

Subject headings: stars: coronae — ultraviolet: stars — X-rays: stars

1. INTRODUCTION

The million degree solar corona radiates mainly in the $\frac{1}{4}$ keV soft X-ray band. Yet, long before the Sun was imaged in X-rays, the remarkable high temperature of the corona was confirmed when Edlén (1945) identified mysterious optical emissions at eclipse as forbidden transitions of highly stripped iron (the so-called red and green lines of Fe X and Fe XIV, respectively). Later, with the deployment of orbiting solar ultraviolet observatories (particularly the *Solar Maximum Mission* and the Apollo Telescope Mount [ATM] on *Skylab*), many coronal forbidden lines were rec-

ognized in the 1150–1700 Å far-UV interval (Doschek et al. 1975; Sandlin, Brueckner, & Tousey 1977; Mason et al. 1986). More recently, the imaging UV spectrometer SUMER on the *Solar and Heliospheric Observatory* (*SOHO*) has identified additional features in long integrations above the solar limb in both quiet areas and magnetic active regions (Feldman et al. 1997, 2000).

On the stellar side, the solar flare line Fe XXI $\lambda 1354$ was discovered in *Hubble Space Telescope* (*HST*) Goddard High-Resolution Spectrograph (GHRS) observations of the dMe star AU Microscopii (M0 V) by Maran et al. (1994) and subsequently in the hyperactive RS Canum Venatic-

rum binary HR 1099 (K1 IV+G5 V) by Robinson et al. (1996) and in Capella (α Aur; G8 III+G1 III)¹ by Linsky et al. (1998). More recently, Johnson et al. (2002) compared *HST* observations of Capella 4 yr apart and found that the previously strong Fe xxI λ 1354 emission of the G8 star in the GHRS spectrum had faded into invisibility in the STIS epoch, while the G1 component was relatively unchanged.

Jordan et al. (2001) identified the magnetic dipole line Fe xII λ 1242 (and its fainter companion at 1349 Å) in a high signal-to-noise Space Telescope Imaging Spectrograph (STIS) observation of the nearby dwarf ϵ Eridani (K2 V), and found evidence of Fe xII in archival STIS echellograms of several other active dwarfs. Young et al. (2001) reported a bright coronal forbidden line—Fe xviii λ 974—in a *Far-Ultraviolet Spectroscopic Explorer (FUSE)* spectrum of Capella. And, in a connection to the early optical solar work of Edlén and others, Schmitt & Wichmann (2001) were able to detect the Fe xiii λ 3388 coronal forbidden line from the ground in the red dwarf CN Leo (M6 V).

A STIS observation of HR 1099 in 1999 September, in conjunction with a long pointing by the *Chandra X-Ray Observatory*, utilized Fe xxI λ 1354 to probe coronal dynamics in a sequence of 14 exposures of \sim 15 minutes each over a period of about 7 hr (Ayres et al. 2001). No coronal flares were evident in light curves from the *Chandra* High-Energy Transmission Grating Spectrometer (HETGS) during that interval, although two striking UV-dominated events were

recorded. The Fe xxI line was relatively “quiet” during the STIS observation, closely following the orbital motion of the K1 subgiant primary, but λ 1354 did show a trend of increasing redshift interrupted by a transient \sim 20 km s⁻¹ blueshift at the peak of the first UV flare.

Figure 1 depicts the spectral context of the faint Fe xII λ 1349 and Fe xxI λ 1354 features in the particularly favorable case of the dM3e flare star AD Leonis, based on a multiwavelength flare campaign in 2000 March by S. Hawley and collaborators in which 52 ks of exposure in the STIS medium-resolution echelle mode was obtained (see Allred et al. 2002). The coronal features are weak compared with neighboring low-excitation narrow chromospheric emissions, which in turn are quite faint compared with the dominant resonance lines and multiplets of the 1200–1700 Å interval.

Nevertheless, the ultraviolet coronal forbidden lines are important in solar work because they can be observed in the disk spectrum of the Sun, outside eclipse, thanks to the faintness of the photospheric continuum below 1700 Å. The same consideration renders these features accessible in distant, unresolved stars. Furthermore, the UV coronal forbidden lines suffer much lower continuum absorption than coronal permitted lines, such as Mg x λ 625, that fall within the H I Lyman continuum (\sim 200–912 Å). This allows probes of localized coronal processes that might be occurring deep in the atmosphere, at chromospheric levels, but which otherwise would be hidden by overlying neutral hydrogen absorption. The ultraviolet coronal forbidden lines can be observed with high-velocity resolution on an absolute wavelength scale. A less satisfactory state of affairs applies to the soft X-ray band, where the dominant emis-

¹ The G8 III star is designated the primary (α Aur Aa) by virtue of its slightly larger mass. The G1 III star is the spectroscopic secondary (α Aur Ab).

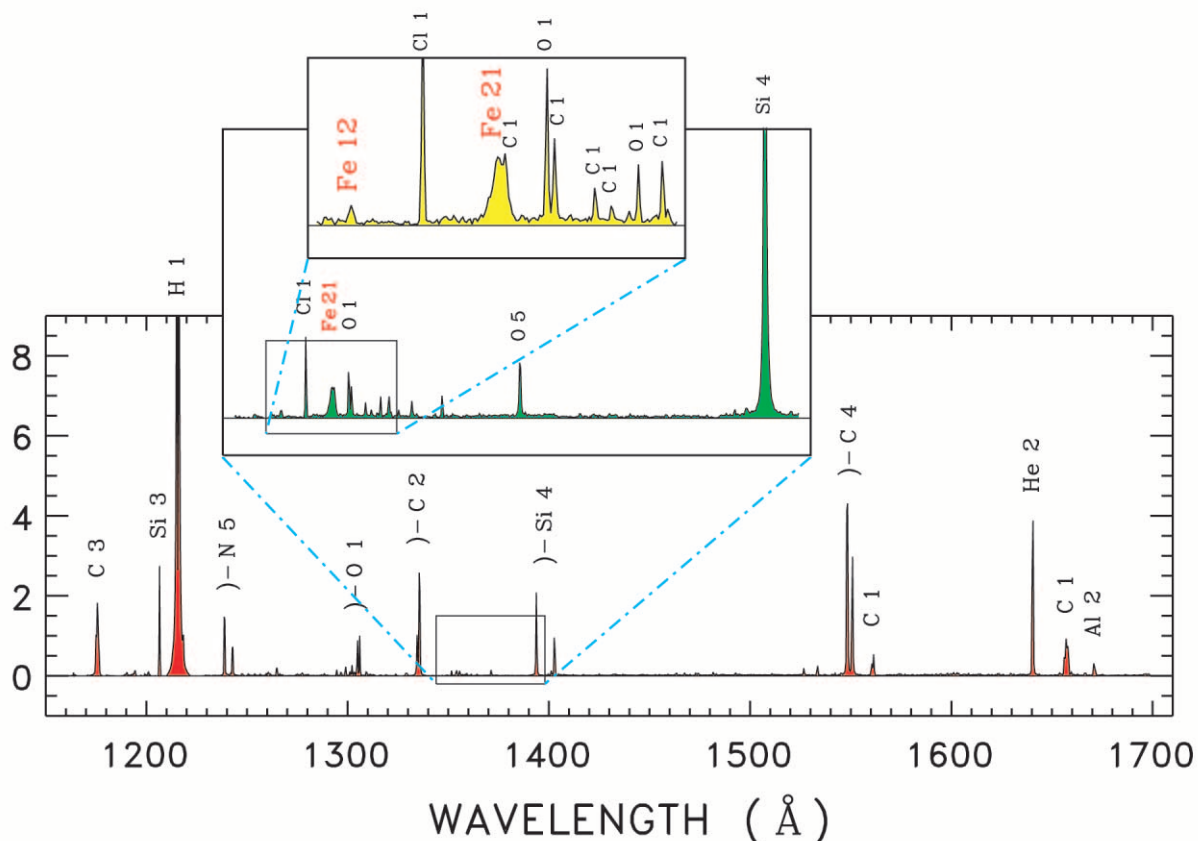


FIG. 1.—Spectral context of the Fe xII λ 1349 and Fe xxI λ 1354 coronal forbidden lines in the dM3e flare star AD Leonis

sions of coronal plasmas fall but spectrograph technology is less mature.

Detecting bulk flows at high temperatures is a vital part of understanding the plasma energy balance in the magnetic loop systems that support and heat the coronal gas on the Sun and presumably other late-type stars as well. Thus, the ultraviolet coronal forbidden lines should play an important role in ferreting out the mechanisms responsible for depositing energy into the corona, widely sought over the past several decades but still elusive.

Because the UV coronal forbidden lines are weak, they are more susceptible to accidental blends than their permitted counterparts in the X-ray band. For example, Fe XII $\lambda 1242$ ($T \sim 2 \times 10^6$ K), which is seen in the disk spectrum of the quiet corona, falls just shortward of much brighter N V $\lambda 1242$. N V forms at cooler “transition zone” (or “sub-coronal”) temperatures ($T \sim 2 \times 10^5$ K), in perhaps an entirely different kinematic environment. A coincidental transition zone “explosive event” (Dere, Bartoe, & Brueckner 1989) in N V could swamp the Fe XII line with high-velocity blue-wing emission from the lower temperature ion. Similarly, Fe XXI $\lambda 1354$ ($T \sim 1 \times 10^7$ K), which is seen only in active region loops and solar flares, is blended in its red wing with a weak chromospheric emission line of C I, thanks partly to the large thermal Doppler broadening of the coronal feature. On the other hand, Fe XII $\lambda 1349$, the weaker component of the $\lambda 1349/\lambda 1242$ pair, falls in a relatively clean part of the spectrum and thus potentially is more valuable for dynamical studies (Mason et al. 1986).

The present paper describes an inventory of the Fe XII and Fe XXI features in late-type (F–M) stars, for which suitable spectral material is available from the *HST* archives, and a search for additional coronal forbidden lines of other species. A companion study (Redfield et al. 2003) describes a similar effort applied to the 900–1190 Å *FUSE* range.

2. OBSERVATIONS

Since its installation in *HST* in 1997, the Space Telescope Imaging Spectrograph (Woodgate et al. 1998) has accumulated a remarkable collection of ultraviolet spectra of stars and other celestial objects. In its far-UV medium-resolution echelle mode (E140M: $\lambda/\Delta\lambda \sim 4 \times 10^4$), STIS can obtain a high signal-to-noise “atlas” of the 1150–1710 Å spectrum in exposures of only a few orbits’ duration (typically <10 ks).

2.1. The Sample

The observations described here come partly from an extensive survey of late-type stars conducted during *HST* Cycle 8 (program 8280), covering the period 1999 May 1 to 2000 October 3. During the program, STIS recorded 13 representative F–K dwarfs, giants, and supergiants. For each target, almost three-quarters of the total exposure time was in the E140M mode. Owing to the deep exposures in the 1150–1710 Å interval, the program 8280 spectra are well suited for the present survey. Added to that sample are numerous Guest Observer (GO) and Guaranteed Time Observer (GTO) observations by our group, or others that have become available in the *HST* public archive.

Table 1 provides summary information for the sample, abstracted from SIMBAD. Figure 2 places the survey targets in the H–R diagram. The left-hand panel displays as bubbles $R_X \equiv L_X/L_{\text{bol}}$ ratios of the targets, according to the

legend. (The normalized flux, sometimes called an activity “index,” is free of the twin biases of stellar distance and radius.) The right-hand panel identifies the individual objects using the key in Table 1. The region encompassed by hatched lines approximately outlines the Hertzsprung gap, through which upper main-sequence stars pass rapidly during their post–main-sequence evolution; the oval marks the “clump,” where post–helium-flash stars congregate for the long-lived core helium burning phase; and the upper shaded zone is occupied by windy “noncoronal” class III giants (Linsky & Haisch 1979) and “hybrid chromosphere” supergiants (Hartmann, Dupree, & Raymond 1980).

2.2. Observing Strategy

Table 2 provides summary information concerning the STIS pointings (and GHRS in the case of α Aur). Many of the observations are from program 8280, which will be described fully in a future paper; a brief outline of the observing strategy will be provided here.

Initial acquisition of the star was performed by the STIS CCD with a narrowband filter, followed by a peakup with the $0''.2 \times 0''.05$ ND slit to accurately center the target. The high-throughput $0''.2 \times 0''.2$ aperture was used for the subsequent E140M exposures, yielding an effective resolution of $R \sim 4 \times 10^4$. The total E140M integration for each star typically was ~ 10 ks, divided into several subexposures usually of duration one orbit (~ 3 ks) each. Archival observations from other programs might have used a somewhat different strategy, but most were conducted in the default E140M mode with the $0''.2 \times 0''.2$ aperture, so typically they are quite comparable to those of program 8280. The major differences would be in the choice of exposure time. We did have to discard one target (36 Oph) because the exposure was too short to provide any useful information concerning the weak coronal forbidden lines. For bright solar twin α Cen A, observations were obtained in the high-resolution echelle mode (E140H; $R = 1.1 \times 10^5$) in three partly overlapping settings to cover the full 1150–1730 Å interval accessible to the “solar-blind” FUV/MAMA detector.

2.3. Spectral Reductions

The E140M and (E140H) echellograms were processed with the IDL-based CALSTIS package developed by the STIS instrument team at Goddard Space Flight Center (Lindler 1999). It successfully removes scattered light contributed by the intense H I Ly α feature and other bright lines, which can affect fainter emissions in nearby echelle orders. The two GHRS pointings were calibrated by the *HST* archive “On-the-Fly” system.

Zero-point corrections to the STIS wavelength scales were based on Pt–Ne lamp exposures taken intermittently during each observation. The first exposure of a sequence will have the most accurate wavelength scale because the narrow-aperture peakup performed immediately prior to the $0''.2 \times 0''.2$ exposure ensured that the target was well centered. Subsequent exposures could deviate owing to accumulation of slow drifts of the target in the aperture. The first exposure therefore was adopted as a reference, and the later spectra were cross-correlated against it to establish any systematic shifts. By comparing large swaths (1300–1340 Å) of the highly structured far-UV region, shifts could be determined to a few hundredths of a pixel (1 pixel = 3.3 km s^{-1}). Typical shifts were less than a pixel, usually only a few

TABLE 1
SURVEY TARGETS

ID (1)	Name (2)	HD or Other (3)	Spectral Type (4)	V (mag) (5)	$B-V$ (mag) (6)	f_{bol} (10^{-7} cgs) (7)	d (pc) (8)	$(v_{\text{rad}})_{\text{obs}}$ (km s^{-1}) (9)
1.....	ζ Dor	33262	F7 V	+4.72	0.52	3.4	11	+0.5
2.....	χ^1 Ori	39587	G0 V	+4.41	0.59	4.7	8.7	-15.6
3.....	α Cen A	128620	G2 V	-0.01	(0.69)	283	1.3	-22.9
4.....	κ Cet	20630	G5 V	+4.83	0.68	3.3	9.2	+18.4
5.....	τ Cet	10700	G8 V	+3.50	0.72	11.3	3.6	-16.9
6.....	ξ Boo A	131156	G8 V	+4.55	0.77	4.5	6.7	+1.5
7.....	70 Oph	165341	K0 V	+4.03	0.86	7.8	5.1	-6.8
8.....	ϵ Eri	22049	K2 V	+3.73	0.88	10.4	3.2	+18.0
9.....	AU Mic	197481	M0 V	+8.61	1.44	0.3	9.9	-3.7
10.....	AD Leo	GJ 388	M3.5 V	+9.43	1.54	0.2	4.7	+12.5
11.....	EV Lac	GJ 873	M3.5 V	+10.06	1.57	0.2	5.0	+0.9
12.....	Proxima Cen	GJ 551	M5.5 V	+11.05	1.97	0.3	1.3	-20.3
a.....	HR 1099	22468	K1 IV + dG	+5.91	0.92	1.5	28	-59.7
b.....	ν Peg	220657	F8 III	+4.40	0.61	5.2	53	-6.0
c.....	31 Com	111812	G0 III	+4.94	0.67	3.4	94	+3.6
d.....	35 Cnc	72779	G0 III	+6.58	0.68	0.9	180	+42.7
e.....	HR 9024	223460	G1 III	+5.90	(0.79)	1.6	140	-2.8
f.....	24 UMa	82210	G4 III	+4.57	0.77	4.6	32	-26.8
g.....	μ Vel	93497	G5 III + dF	+2.72	0.90	28	35	+6.6
h.....	α Aur Ab	34029b	G1 III	+0.76	0.65	138	12	+58.1
i.....	α Aur Aa	34029a	G8 III	+0.91	0.88	140	12	(+5.1)
j.....	ι Cap	203387	G8 III	+4.30	0.90	6.8	66	+12.0
k.....	β Cet	4128	K0 III	+2.04	1.02	56	29	+13.3
l.....	α Boo	124897	K1.5 III	-0.04	1.23	453	11	-4.6
m.....	α Tau	29139	K5 III	+0.85	1.54	343	19	+54.2
α	α TrA	150798	K2 II	+1.92	1.44	106	130	-3.4
β	β Aqr	204867	G0 Ib	+2.91	0.83	26	190	+7.1
γ	β Cam	31910	G1 Ib	+4.03	0.93	11.8	300	-0.6
δ	ϵ Gem	48329	G8 Ib	+3.02	1.40	41	280	+7.1

NOTE.—Col. (1) is an identification symbol used in Fig. 2. Cols. (2)–(6) and (8) are from SIMBAD. Estimate of apparent bolometric luminosity, f_{bol} in $\text{ergs cm}^{-2} \text{s}^{-1}$ at Earth (col. [7]) was derived from the visual magnitude V - and $B-V$ -dependent bolometric correction, with a distance-dependent compensation for interstellar reddening (see, e.g., Ayres et al. 1998). The stellar luminosity is $L_*/L_{\odot} \sim 3.13 \times 10^{-3} f_{\text{bol}} (10^{-7}) d^2$ (pc). The observed radial velocity in the final column was based on an average of low-excitation chromospheric lines and refers to the apparent dominant emitter in the case of a binary system (and to the velocity at the epoch of observation). Typical uncertainties (1 s.e.) in $(v_{\text{rad}})_{\text{obs}}$ are better than $\pm 0.5 \text{ km s}^{-1}$ ($\pm 1 \text{ km s}^{-1}$ for broad-line stars b, c, and d). The velocity for Capella G8 was derived from the measured value of G1 according to the predicted relative orbital shift at 53 km s^{-1} at $\phi = 0.73$.

tenths. Finally, each spectrum was registered to the reference wavelength scale and co-added. In the case of HR 1099, which experienced two UV flares during the STIS observation, we included only the six “quiescent” frames (each ~ 0.9 ks), of 14 total, described by Ayres et al. (2001). For the narrow-line dwarf stars, the agreement between the average velocity of low-excitation chromospheric emissions in the co-added spectrum and the stellar radial velocity (derived from photospheric absorption lines in the visible) generally was better than 1 km s^{-1} , with no systematic trends over the sample.

In the case of α Cen, the three high-resolution echelle observations were cross-correlated in the regions of overlap to align the second spectrum to the first and the third to the second. The concatenated spectrum then was convolved with a $\text{FWHM} = 7.5 \text{ km s}^{-1}$ Gaussian to simulate the resolution of the E140M mode.

The two GHRS spectra for α Aur, covering $\sim 35 \text{ \AA}$ intervals centered at 1360 and 1655 \AA , have somewhat higher flux levels than the STIS E140M spectrum, by factors of 1.26 and 1.14, respectively (measured in continuum-dominated regions; see also Johnson et al. 2002). The STIS observations used a narrow echelle slit, only $0''.06$ in the dis-

persion direction, instead of the $0''.2$ of the default “photometric” aperture. The GHRS spectra, on the other hand, were taken through the $2'' \times 2''$ Large Science Aperture utilizing the COSTAR corrective optics, so there is no reason to doubt their flux scales. Although we cannot rule out intrinsic continuum emission changes in the binary itself, we chose to attribute the diminished STIS flux levels to slight errors in the aperture calibration tables and rescaled the corresponding STIS intervals to the two GHRS flux scales by the factors mentioned previously.

3. ANALYSIS

Figure 3 is a montage of STIS survey spectra in a wavelength range containing both the Fe XII $\lambda 1349$ and Fe XXI $\lambda 1354$ coronal forbidden lines. The traces were smoothed with a Gaussian filter of $\text{FWHM} = 3$ pixels for the dwarfs, 4 for the slowly rotating giants, up to 15 for the fast-rotating Hertzsprung-gap stars, and 6 for the broad-line supergiants. (The filtering increases the signal-to-noise ratio [S/N] without significantly affecting the line shapes.) The flux scales were adjusted to match the general levels of the chromospheric C I features between each star. In the less active stars

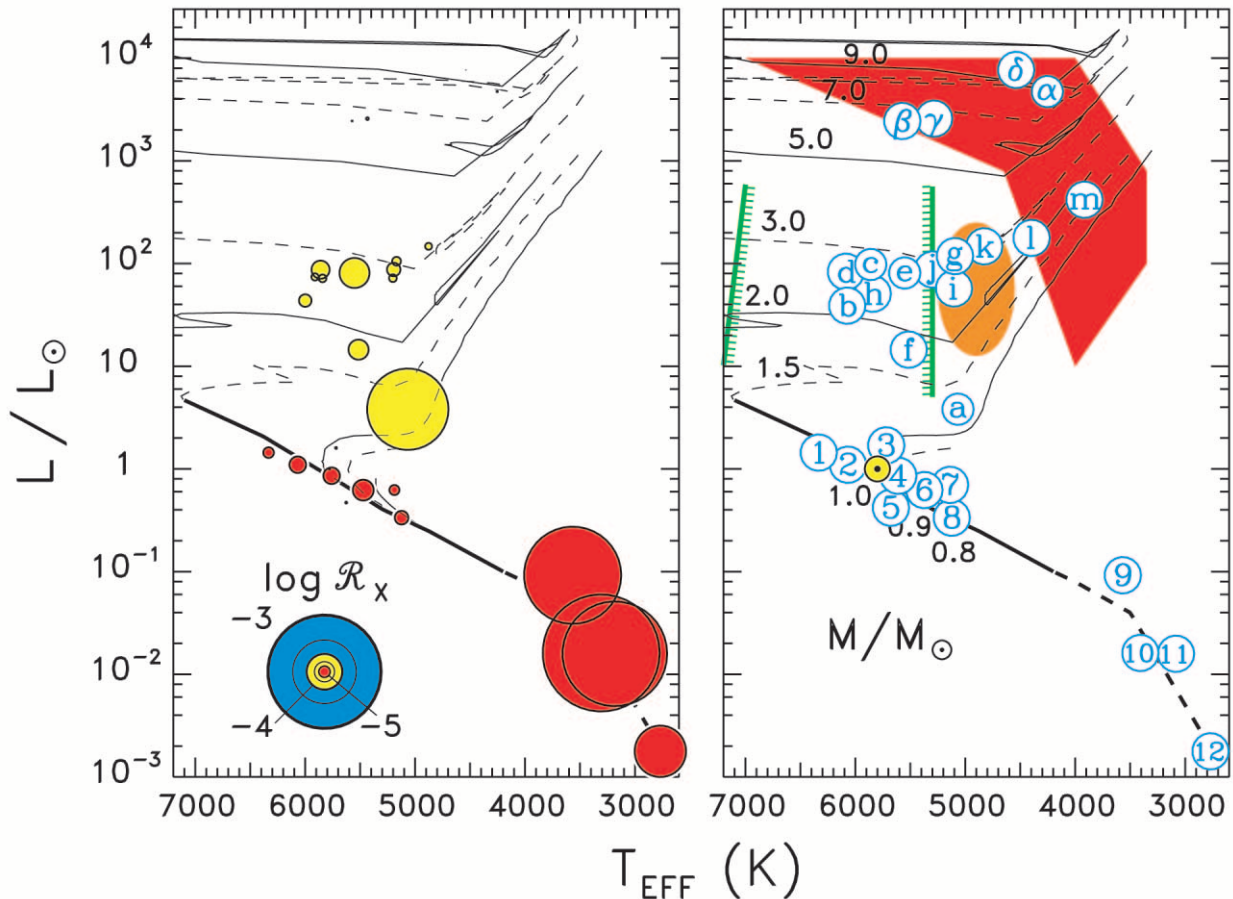


FIG. 2.—Location of survey targets in the H-R diagram. The left-hand panel displays as bubbles $\mathcal{R}_x \equiv L_x/L_{\text{bol}}$ ratios of the stars, according to the legend. The right-hand panel identifies the individual objects according to the key provided in Table 1. The region encompassed by hatched lines approximately outlines the Hertzsprung gap, the oval marks the core helium burning “clump,” and the upper shaded zone is occupied by windy “noncoronal” class III giants and “hybrid chromosphere” supergiants at higher luminosities.

(e.g., α Cen, τ Cet, α Boo), Fe xxI is absent and the C I $\lambda 1354$ line can be seen in isolation. In the high-luminosity supergiants, a weak feature, possibly Cr II, appears between Fe xxI and C I. (Note, also, the Cr II feature near 1348.7 Å, which strengthens dramatically in the cooler supergiants. It likely is fluorescent, pumped through Cr II $\lambda 1214.294$ by H I Ly α .)

Capella is represented by the recent STIS spectrum (1999 September) and the GHRS G160M observation taken almost exactly 4 yr earlier at the same orbital phase ($\phi = 0.73$; G8 star 53 km s $^{-1}$ to the blue of the G1 star). The GHRS resolution is a factor of 2 lower than STIS. Notice in the STIS spectrum the sharp component in the blue wing of O I $\lambda 1355$, contributed by the narrow-line G8 star. In C I $\lambda 1351$, however, the G8 contribution is more subdued. The C I line is radiatively pumped by C II $\lambda 1335$ (Shine 1975). The C II spectrum is doubly weakened in the G8 star, both because its transition zone emissions are faint compared with the Hertzsprung-gap G1 star (Ayes & Linsky 1980) and because its carbon abundance is probably also depressed owing to dredge-up dilution during the first ascent of the giant branch (e.g., Day, Lambert, & Sneden 1973).

It is clear that Fe XII and Fe XXI appear in a number of the survey stars, particularly those known to be coronally active on the basis of elevated soft X-ray fluxes: dMe stars, β Cet-like clump giants, and the RS CVn binary HR 1099. We next examined whether coronal forbidden lines from other species might be visible as well.

3.1. General Search for UV Coronal Forbidden Lines

We developed a list of nearly 50 candidate coronal forbidden lines in the 1200–1600 Å interval from recent *SOHO* work (Feldman et al. 2000), earlier *Skylab* ATM studies (e.g., Sandlin, Brueckner, & Tousey 1977), and atomic line lists (particularly “The Atomic Line List v2.04,” hosted by the department of Physics and Astronomy, University of Kentucky). Candidate lines were restricted to ground-state transitions of species expected to be abundant in coronally active stars. To enhance our ability to recognize subtle features, we co-added selected spectra in two classes: (1) active dwarfs, including the dKe and dMe stars 70 Oph, ϵ Eri, AU Mic, AD Leo, and Proxima Cen; and (2) active G/K giants, including HR 9024, 24 UMa, μ Vel, ι Cap, and β Cet. Both groups display strong Fe XXI features. The active dwarfs, particularly the dKe stars, show prominent Fe XII as well. The absence of Fe XII in the active giants is understandable, given the weakness of their coronal emission measure distributions in the $(1\text{--}3) \times 10^6$ K range (Dupree, Brickhouse, & Hanson 1996; Ayres et al. 1998).

Figures 4a and 4b present a series of spectral snapshots at the predicted locations of the target coronal forbidden lines. The species are ordered from top to bottom in decreasing elemental cosmic abundance and, within a particular species, in increasing wavelength from left to right. The green and orange shaded profiles refer to the low-activity

TABLE 2
JOURNAL OF *HST* OBSERVATIONS

Star Name	Data Set Root	UT Date	Exposure Time (ks)	Notes
ζ Dor	o5bn01	1999 May 1	6.00	
χ^1 Ori.....	o5bn02	2000 Oct 3	6.77	
α Cen A.....	o53p01	1999 Feb 12	14.09	E140H/1238, 1416, 1598; 0.2×0.09
κ Cet.....	o5bn03	2000 Sep 19	7.81	
τ Cet.....	o5cy01	2000 Aug 1	13.45	
ξ Boo A.....	o4vb51	1998 Dec 16	2.45	0.2×0.06
70 Oph.....	o5bn05	2000 Aug 23	7.81	
ϵ Eri.....	o55p01	2000 Mar 17	5.80	
AU Mic.....	o4z301	1998 Sep 6	10.11	
AD Leo.....	o61s0n	2000 Mar 10	52.00	$n = 1-4$
EV Lac.....	o6au01	2001 Sep 20	10.92	
Proxima Cen.....	o5eo0n	2000 May 8	41.16	$n = 1-2$
HR 1099	o5bn99	1999 Sep 15	12.23	
ν Peg.....	o5bn06	2000 Jul 11	8.23	
31 Com.....	o6aq01	2001 Mar 13	7.73	
35 Cnc.....	o5bn10	2000 May 11	11.70	
HR 9024	o5bn20	2000 May 17	12.08	
24 UMa.....	o5bn31	2000 Feb 24	9.30	
μ Vel.....	o6aq02	2001 Sep 25	8.50	
α Aur.....	o5lc01	1999 Sep 12	8.11	0.2×0.06
	z2uw0207p	1995 Sep 9	1.09	G160M/1654; 2.0
	z2uw0209n	1995 Sep 9	9.79	G160M/1361; 2.0
ι Cap.....	o5bn40	2000 Apr 15	11.65	
β Cet.....	o5b701	1999 Sep 13	4.74	
α Boo.....	o4y701	1998 Aug 24	5.21	0.2×0.06
α Tau.....	o6je01	2002 Jan 3	10.51	
α TrA.....	o5a501	1999 Jul 23	9.00	
β Aqr.....	o5bn50	2000 Apr 16	13.43	
	o5bn51	2000 Apr 28	4.06	
β Cam.....	o5bn60	1999 Sep 19	13.75	
ϵ Gem.....	o5bn70	2000 Mar 9	10.42	

NOTE.—All exposures are in E140M medium-resolution echelle mode, through the $0''.2 \times 0''.2$ aperture, unless otherwise noted. Entries in the final column are “grating/ λ_{cen} ; aperture” or “ $n = 1 - N$ ” for multiple consecutive visits.

solar-like G dwarf α Cen A and the “noncoronal” K giant α Boo, respectively. The red and blue traces represent the co-added spectra of active dwarfs and giants, respectively, described earlier. The individual traces were normalized to the total flux in the interval 1250–1600 Å, after subtracting a continuum level determined by applying specially designed filters (e.g., Bennett & Ayres 1988). The flux ordinate of each panel was chosen to highlight the spectral structure near the predicted forbidden line. A candidate coronal forbidden line would appear in either the active dwarf or active giant summed spectra, or in both, but not in either of the quiet stars (at least not at a comparable intensity). By this criterion, for example, Ca xiv λ 1291 and λ 1432 are excluded. An additional signature of a coronal forbidden line would be its anomalous width, due to the substantial thermal broadening in the hot corona, compared with species arising in the ~ 1000 times cooler underlying chromosphere.

Careful examination revealed only a very few plausible candidates beyond the known Fe xii and Fe xxi features. In some cases, Ar xiii λ 1296 for example, a feature meeting the criteria described above appears close to the predicted coronal forbidden line wavelength, but it is probably a low-temperature transition, in this case Si iii λ 1296.726. After eliminating the obvious low-temperature coincidences, the most promising remaining candidates were Ar xiii λ 1330 (in

the dwarfs) and Ca xv λ 1375 (in the giants). Neither of these, however, is as bright as the known Fe lines: the Ar xiii feature is about 10% the integrated flux of Fe xii λ 1242 in the summed active dwarf spectrum, and Ca xv also is about 10% the strength of Fe xxi in the summed active giant spectrum. Thus, their diagnostic potential cannot be considered high (except, perhaps, from the point of view that Ar xiii is a high-FIP [first ionization potential] species, whereas Fe and Ca are low-FIP; the low-FIP elements tend to be enhanced in the solar corona by a factor of up to 4 relative to the high-FIP species [e.g., Feldman & Laming 2000], by an unknown fractionation process).

3.2. A Closer Look at Fe xii and Fe xxi

Given the somewhat disappointing inventory of coronal forbidden line candidates, we decided to focus our attention on the Fe xxi λ 1354 feature. It is the most prominent of the three coronal Fe lines in many of the stars and a tracer of hot plasmas ($T \sim 10^7$ K). The latter characteristic would be especially important for exploring kinematics associated with transient flare events on active stars. The main obstacle in the practical use of the Fe xxi line is the blend in its long-wavelength wing with a weak chromospheric emission line of atomic carbon (1354.288 Å). Appendix A describes our empirical approach to compensate for the C i blend.

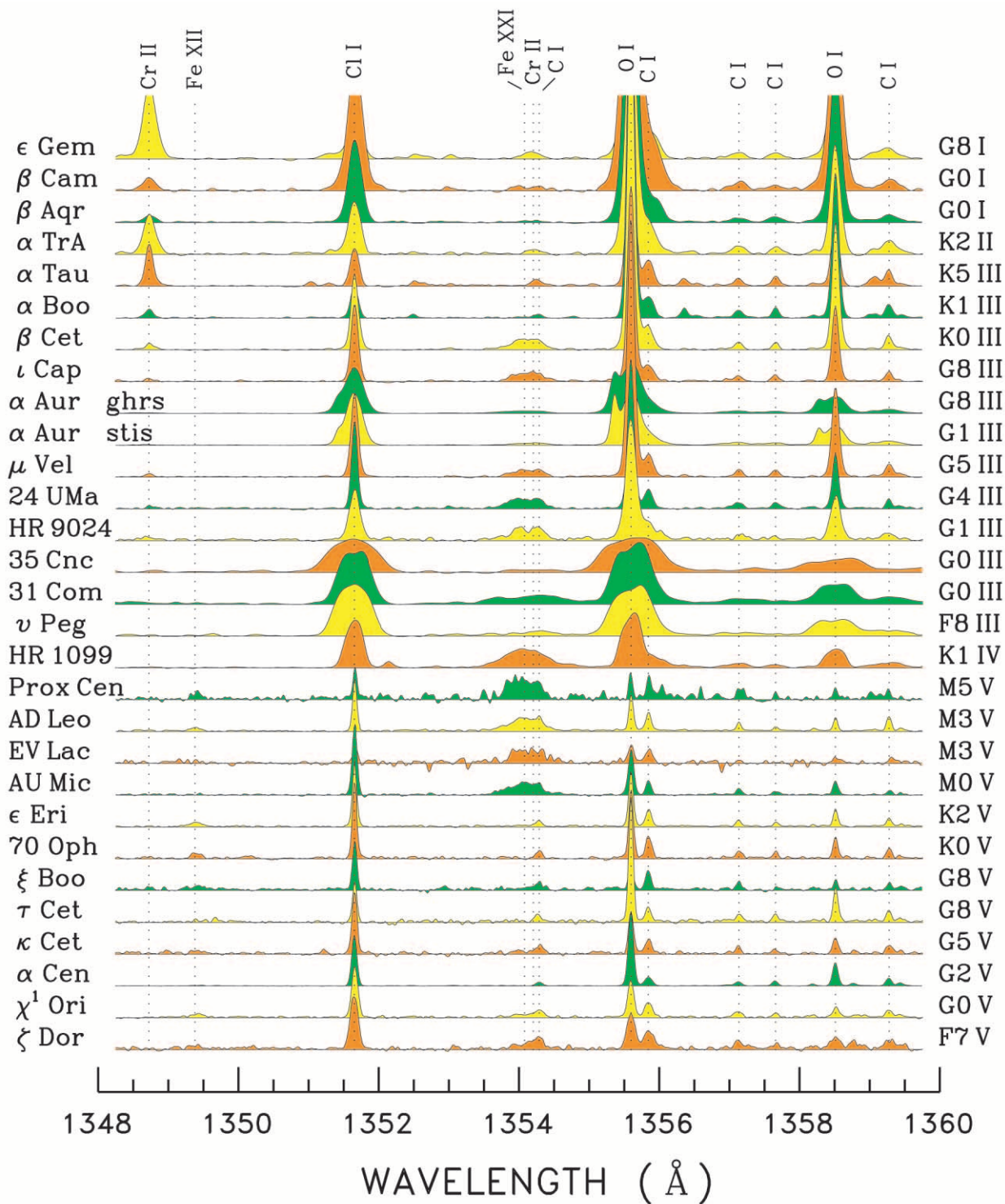


FIG. 3.—Montage of far-UV survey spectra in a wavelength interval containing both the Fe XII $\lambda 1349$ and Fe XXI $\lambda 1354$ coronal forbidden lines. The flux scales were adjusted to approximately equalize the central intensities of the low-excitation chromospheric C I lines. Capella (α Aur) is represented by a recent STIS spectrum (1999 September) and a GHRS G160M observation taken 4 yr earlier.

Figure 5 illustrates the result of superposing the scaled Fe XXI $\lambda 1354$ profiles of seven stars, mostly G1–K0 giants but including two M dwarfs, after correcting for the C I blend. The individual line shapes in some cases display significant structure, but collectively they define a “universal” profile that can be matched by a Gaussian with FWHM $\sim 110 \text{ km s}^{-1}$ and an essentially negligible 2 km s^{-1}

blueshift (with respect to the predicted average photospheric velocities of the stars and the adopted wavelength of the Fe XXI line, 1354.080 \AA).

Figure 6 presents a montage of Fe XXI profiles before (*left*) and after (*right*) correcting for the C I blend. The red asterisks (*to the right of the spectral types*) mark the stars that we consider to have positive detections of Fe XXI. Note the

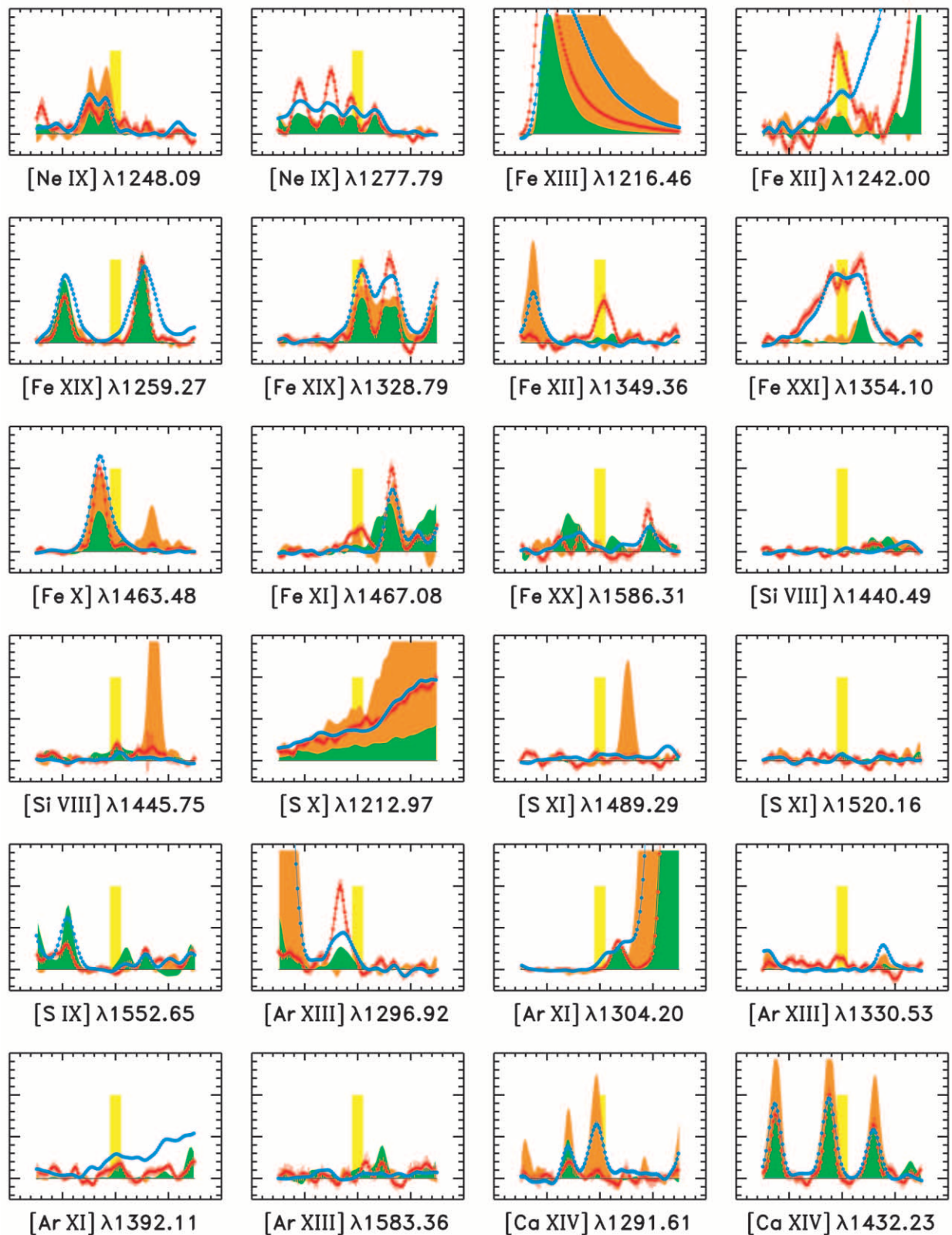


FIG. 4a

FIG. 4.—(a) Snapshots at predicted locations of candidate coronal forbidden lines known from the solar spectrum, or taken from atomic line lists. Transitions are ordered from top to bottom in decreasing parent species cosmic abundance and, within a particular element, in increasing wavelength from left to right. Large ticks in the abscissa mark 0.5 \AA increments, relative to the predicted wavelength (indicated by the vertical yellow stripe). Green and orange shaded profiles refer to the low-activity solar twin α Cen A (G2 V) and the noncoronal red giant α Boo (K1 III), respectively. Red and blue traces represent co-added spectra of active dwarf stars and clump giants, respectively. (b) Same as (a), for additional candidate coronal forbidden lines.

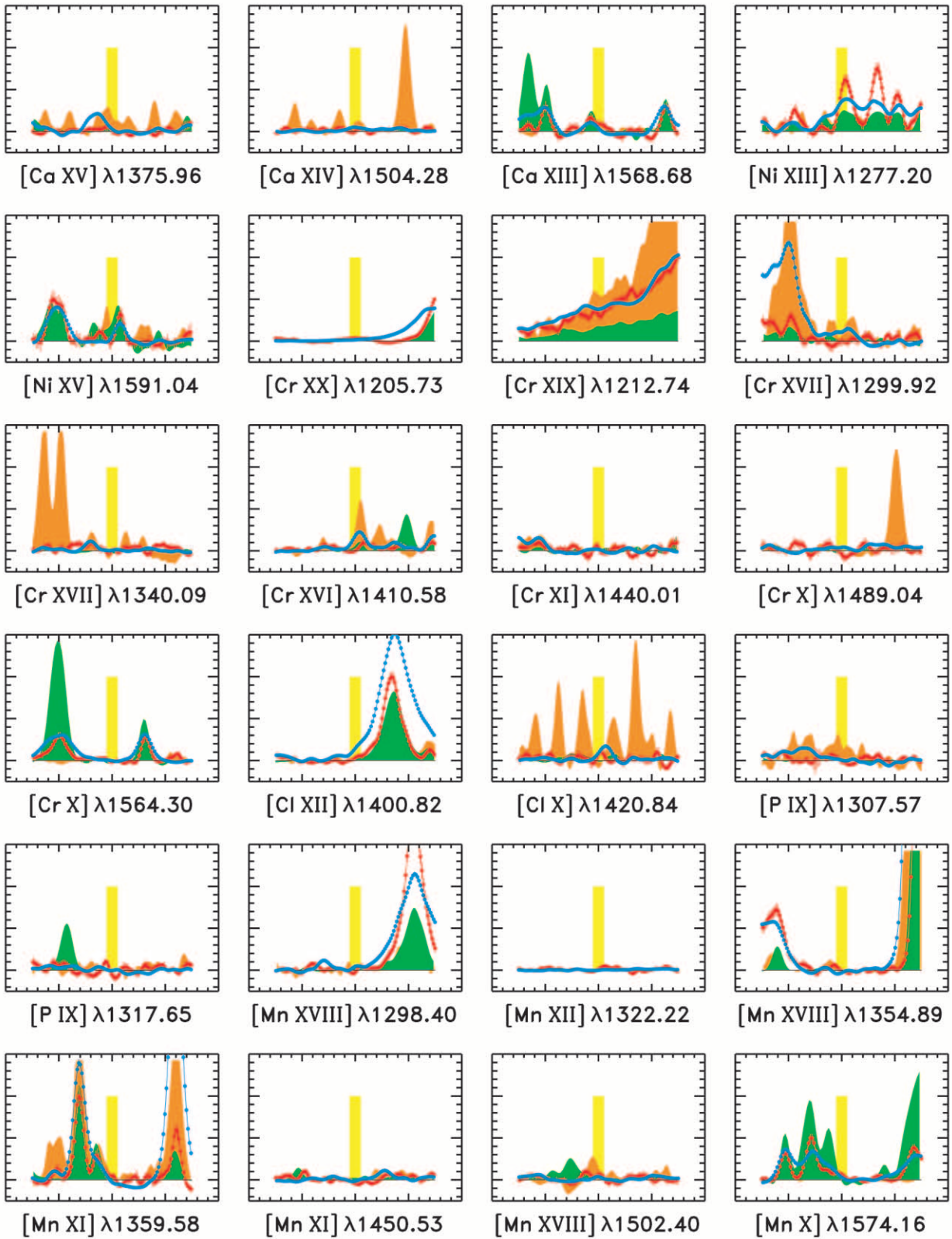


FIG. 4b

dramatic change in the GHRS and STIS profiles of Capella, taken 4 yr apart. Also note the appearance in several of the more luminous targets (e.g., α Tau, α TrA, and ϵ Gem) of the secondary blend at 1354 Å attributed to Cr II.

We measured the deblended Fe xxI features, where present, and included the fluxes in Table 3, together with Fe xII fluxes $\lambda 1242 + \lambda 1349$ for the targets in which the lower temperature coronal emissions were detected. Tables 4

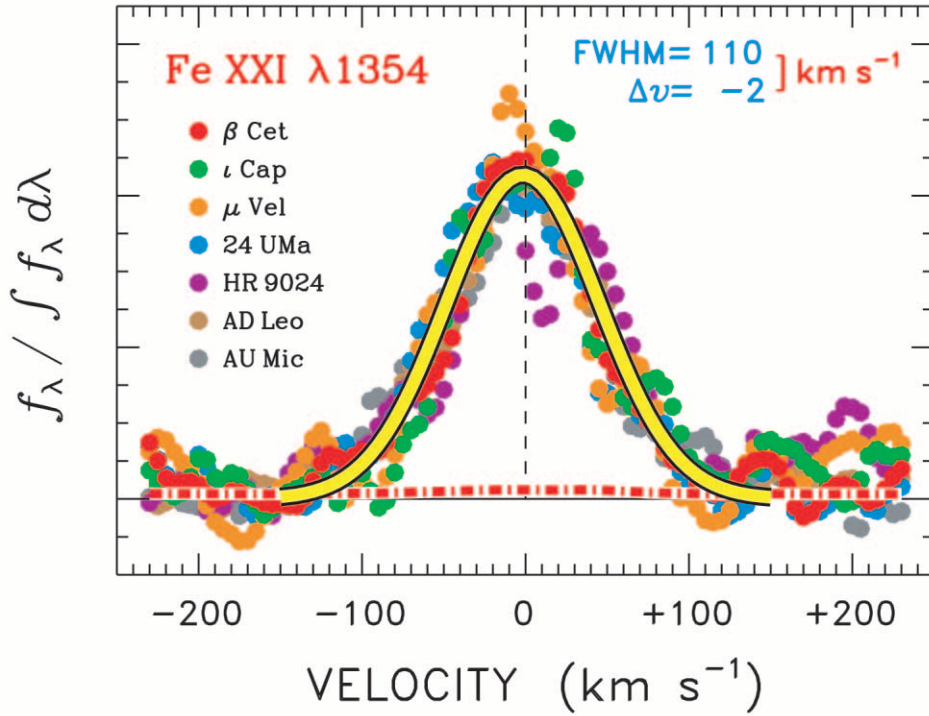


FIG. 5.—Superposition of scaled Fe XXI $\lambda 1354$ profiles. The colored circles refer to individual stellar profiles according to the legend at left. The horizontal red dot-dashed curve indicates a 1 s.e. photometric uncertainty level for the sum. The overlying smooth yellow curve is a Gaussian fit to the mean profile. The FWHM and (negligible) Doppler shift Δv of the fitted profile are listed in the upper right.

and 5 summarize single-Gaussian modeling of the Fe XII $\lambda 1242$ and Fe XXI $\lambda 1354$ profiles, respectively, for the brightest examples in the survey (31 Com was omitted from Table 5 because its Fe XXI profile is flat-topped and decidedly non-Gaussian). Fe XII $\lambda 1349$ generally was too faint for reliable modeling.

Some of the Fe XXI profiles display internal structure that is significant with respect to the photometric noise levels. We doubt that the deviations represent genuine velocity substructure within the profile, because the large thermal widths would tend to wash out any distinct velocity components that might be present. It is equally difficult, however, to make a compelling case for overlying absorption by a neutral or singly ionized species. Regardless of the origin of the profile structure, it does have a major influence on the Gaussian modeling: the fits become sensitive to the choice of which portions of the profile are included in the modeling and which are ignored. For that reason, the FWHM values listed in Table 5 reflect a range of possible profile fits, but the tabulated velocities are for the intermediate case. In all instances, the inferred velocity shifts are small and consistent with the stellar (chromospheric) velocity. For most of the cases, the line widths appear close to thermal (FWHM [Fe XII] ~ 41 km s $^{-1}$ at 2×10^6 K; FWHM [Fe XXI] ~ 91 km s $^{-1}$ at 10^7 K).

The case of Capella is a special one owing to the orbital Doppler shifting of the stellar Fe XXI components and the two independent epochs of observations. Our strategy for measuring the individual contributions from the Capella stars, and the results of a variability analysis, are described in Appendix B.

4. DISCUSSION

4.1. Flux-Flux Diagrams

Figure 7 represents one of the main results of our efforts: a flux-flux (or “correlation”) diagram comparing measured coronal forbidden iron fluxes, and upper limits, for the stars of our sample with available *ROSAT* PSPC X-ray detections (0.2–2 keV; see Table 3 and Appendix C). The dashed green lines are illustrative power laws adjusted to match the higher X-ray luminosity objects and guide the eye to deviations among the others. The Fe XII fluxes were confined solely to the dwarfs of the sample because broad N V $\lambda 1242$ features in the giants render detection of faint Fe XII problematic and upper limits meaningless. The dwarf stars show an approximately square-root dependence of Fe XII on the *ROSAT* index, while Fe XXI appears to be more linearly correlated, at least for the higher activity objects.

The kinked red line in the right-hand panel connects the GHRS detection of Fe XXI in the Capella primary with a 3σ upper limit deduced from the later STIS observation. The other detections of Fe XXI in G giants of comparable X-ray activity to the Capella primary set an important context for the substantial decline. The change possibly is reminiscent of that seen in the clump giant β Cet in long pointings by the *EUV*E 6 yr apart: in the earlier epoch, the active K giant displayed a relatively flat 80–170 Å light curve (dominated by coronal Fe emissions), while in the later interval (a pointing some 40 days in duration) not only was the overall EUV flux level elevated by a factor of 2, but there was a dramatic sequence of almost continuous flaring (Ayres, Osten, & Brown 2001).

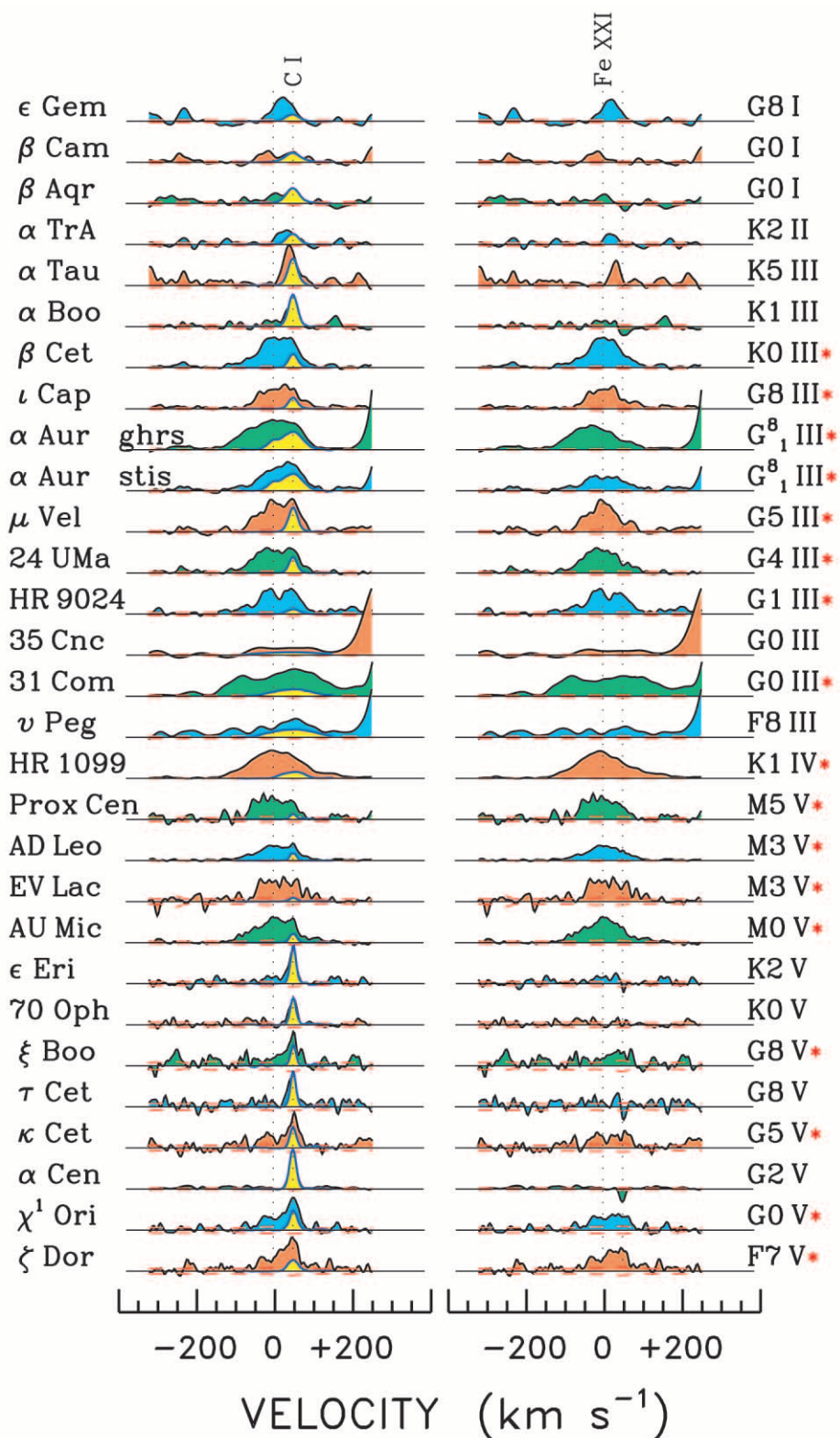


FIG. 6.—Montage of Fe xxI profiles before (*left*) and after (*right*) correction for the C I blend. The red asterisks mark stars with positive detections of Fe xxI features. The horizontal red dashed curves (barely visible in some cases) indicate $\pm 1 \sigma$ photometric uncertainty levels.

The diagram illustrates a good correlation between the Fe xxI coronal forbidden line flux and the soft X-ray index of the star, regardless of stellar type or luminosity class, down to $R_X \equiv L_X/L_{\text{bol}} \sim 2 \times 10^{-5}$. Below that point, only

the clump giants maintain strong Fe xxI, at least for some of the time (with the caveat of Capella's example), while other classes of stars are not detected at present sensitivity levels. Our suspicion is that Fe xxI drops substantially at this

TABLE 3
CARBON, IRON, AND X-RAY FLUXES

Name	C I λ 1354 ($\times 10^{-15}$)	C I λ 1602 ($\times 10^{-15}$)	C I λ 1657 ($\times 10^{-12}$)	Fe XII ($\times 10^{-15}$)	Fe XXI λ 1354 ($\times 10^{-15}$)	X-Rays ($\times 10^{-12}$)
ζ Dor	(1.8)	3.4 \pm 0.9	0.16 \pm 0.01	2.5 \pm 0.6	4.2 \pm 0.4	3 \pm 1
χ^1 Ori	(1.4)	5.0 \pm 0.9	0.22 \pm 0.01	5.3 \pm 0.6	3.5 \pm 0.5	10 \pm 2
α Cen A	10.9 \pm 0.7	44 \pm 2	3.02 \pm 0.02	11.5 \pm 1.4	\lesssim 3	7 \pm 2
κ Cet	1.1 \pm 0.3	3.6 \pm 0.8	0.16 \pm 0.01	3.9 \pm 0.5	2.6 \pm 0.3	7 \pm 1
τ Cet	0.7 \pm 0.2	2.6 \pm 0.5	0.14 \pm 0.01	\lesssim 0.7	\lesssim 0.6	0.3 \pm 0.1
ξ Boo A	1.5 \pm 0.5	3.3 \pm 0.9	0.23 \pm 0.01	5.8 \pm 1.1	4.0 \pm 0.7	15 \pm 2
70 Oph	1.4 \pm 0.2	4.7 \pm 0.6	0.27 \pm 0.01	6.7 \pm 0.5	\lesssim 1.0	6 \pm 1
ϵ Eri	2.4 \pm 0.3	8.0 \pm 0.7	0.49 \pm 0.01	12.0 \pm 0.8	\lesssim 1.5	15 \pm 5
AU Mic	(0.8)	2.1 \pm 0.4	0.120 \pm 0.004	1.3 \pm 0.3	7.5 \pm 0.5	22 \pm 11
AD Leo	(0.8)	3.3 \pm 0.2	0.16 \pm 0.01	2.8 \pm 0.2	7.8 \pm 0.2	25 \pm 6
EV Lac	0.038 \pm 0.004	\lesssim 0.9	4.2 \pm 0.3	17 \pm 10
Proxima Cen	(0.2)	0.8 \pm 0.2	0.025 \pm 0.002	1.2 \pm 0.1	2.0 \pm 0.1	7 \pm 2
HR 1099	1.11 \pm 0.02	...	48 \pm 1	75 \pm 12
ν Peg	0.44 \pm 0.02	...	\lesssim 2	6 \pm 1
31 Com	0.35 \pm 0.02	...	10.3 \pm 0.6	8 \pm 1
35 Cnc	0.09 \pm 0.01	...	\lesssim 1	0.3 \pm 0.1
HR 9024	0.9 \pm 0.3	3.2 \pm 0.7	0.077 \pm 0.004	...	5.0 \pm 0.3	10 \pm 5
24 UMa	0.9 \pm 0.3	4.6 \pm 0.6	0.23 \pm 0.01	...	7.4 \pm 0.4	14 \pm 1
μ Vel	(1.9)	8.7 \pm 1.1	0.64 \pm 0.01	...	11.8 \pm 0.6	16 \pm 1
α Aur (STIS)	11.3 \pm 0.1	...	74 \pm 3	127 \pm 16
α Aur (GHRS)	11.9 \pm 0.1	...	137 \pm 3	127 \pm 16
ι Cap	(1.0)	3.7 \pm 0.6	0.19 \pm 0.01	...	5.9 \pm 0.3	9 \pm 3
β Cet	(3.4)	13.9 \pm 1.4	1.02 \pm 0.02	...	37 \pm 1	20 \pm 2
α Boo	6.8 \pm 0.9	29 \pm 2	1.63 \pm 0.03	...	\lesssim 4	\lesssim 0.02
α Tau	6.6 \pm 0.5	12.3 \pm 1.0	0.74 \pm 0.01	...	\lesssim 2	\lesssim 0.04
α TrA	0.50 \pm 0.03	...	\lesssim 3	0.9 \pm 0.1
β Aqr	0.23 \pm 0.01	...	\lesssim 1	0.1 \pm 0.0
β Cam	0.17 \pm 0.01	...	\lesssim 1	0.5 \pm 0.1
ϵ Gem	0.14 \pm 0.01	...	\lesssim 1	\lesssim 0.1

NOTE.—Fluxes in ergs cm $^{-2}$ s $^{-1}$ at Earth. Values for C I λ 1354 in parentheses were measured after subtracting a scaled mean Fe XXI profile (see Appendix A). The Fe XII and Fe XXI fluxes, or upper limits, were obtained by direct numerical integrations, in a fixed ± 100 km s $^{-1}$ interval for the latter unless the apparent feature was broader. X-ray fluxes refer to the band 0.2–2 keV, derived from material in the *ROSAT* archive as described in Appendix C.

point, reflecting the trend toward cooler coronae with decreasing X-ray index proposed by Güdel, Guinan, & Skinner (1997, hereafter GGS). Fe XII maintains a similarly good, although flatter, correlation with the X-ray index also down to $R_X \sim 10^{-5}$, and even the single detection well below that point (α Cen A at $R_X \sim 3 \times 10^{-7}$) does not depart strongly from the square-root law. The contrasting behavior of Fe XII and Fe XXI with increasing X-ray index likely reflects the growing dominance of a hot ($T > 10^7$ K), flarelike component of the emission measure structure (see GGS).

4.2. Superrotational Broadening of Fe XXI?

Figure 8 compares chromospheric C I λ 1351, subcoronal O V λ 1371, and coronal Fe XXI λ 1354 in slowly rotating β Cet and faster spinning stars including the tidally synchronized RS CVn binary HR 1099 and two Hertzsprung-gap giants, Capella G1 and 31 Com. All three of the spectral lines are expected to be optically thin, particularly semipermitted O V and forbidden Fe XXI, and thus should be reliable tracers of the kinematic environments in which they form. We adopted the β Cet profiles as “zero rotation” references

TABLE 4
FE XII λ 1242 VELOCITY DETAILS

Name	v_L (km s $^{-1}$)	FWHM (km s $^{-1}$)
χ^1 Ori	+2 \pm 2	46 \pm 5
α Cen A	−8 \pm 2	41 \pm 5
κ Cet	−8 \pm 2	46 \pm 4
70 Oph	−1 \pm 1	56 \pm 5
ϵ Eri	−5 \pm 2	50 \pm 4
AD Leo	−2 \pm 2	44 \pm 3
Proxima Cen	−8 \pm 2	46 \pm 5

TABLE 5
FE XXI λ 1354 VELOCITY DETAILS

Name	v_L (km s $^{-1}$)	FWHM (km s $^{-1}$)
AU Mic	−5 \pm 3	112 $^{+10}_{-14}$
AD Leo	+3 \pm 1	108 $^{+5}_{-5}$
HR 1099	−10 \pm 1	136 $^{+11}_{-2}$
HR 9024	+5 \pm 3	108 $^{+11}_{-4}$
24 UMa	−6 \pm 3	112 $^{+4}_{-12}$
μ Vel	−2 \pm 3	106 $^{+8}_{-20}$
α Aur (STIS)	+0 \pm 3	130 $^{+8}_{-15}$
ι Cap	+1 \pm 3	97 $^{+12}_{-6}$
β Cet	−2 \pm 2	102 $^{+3}_{-10}$

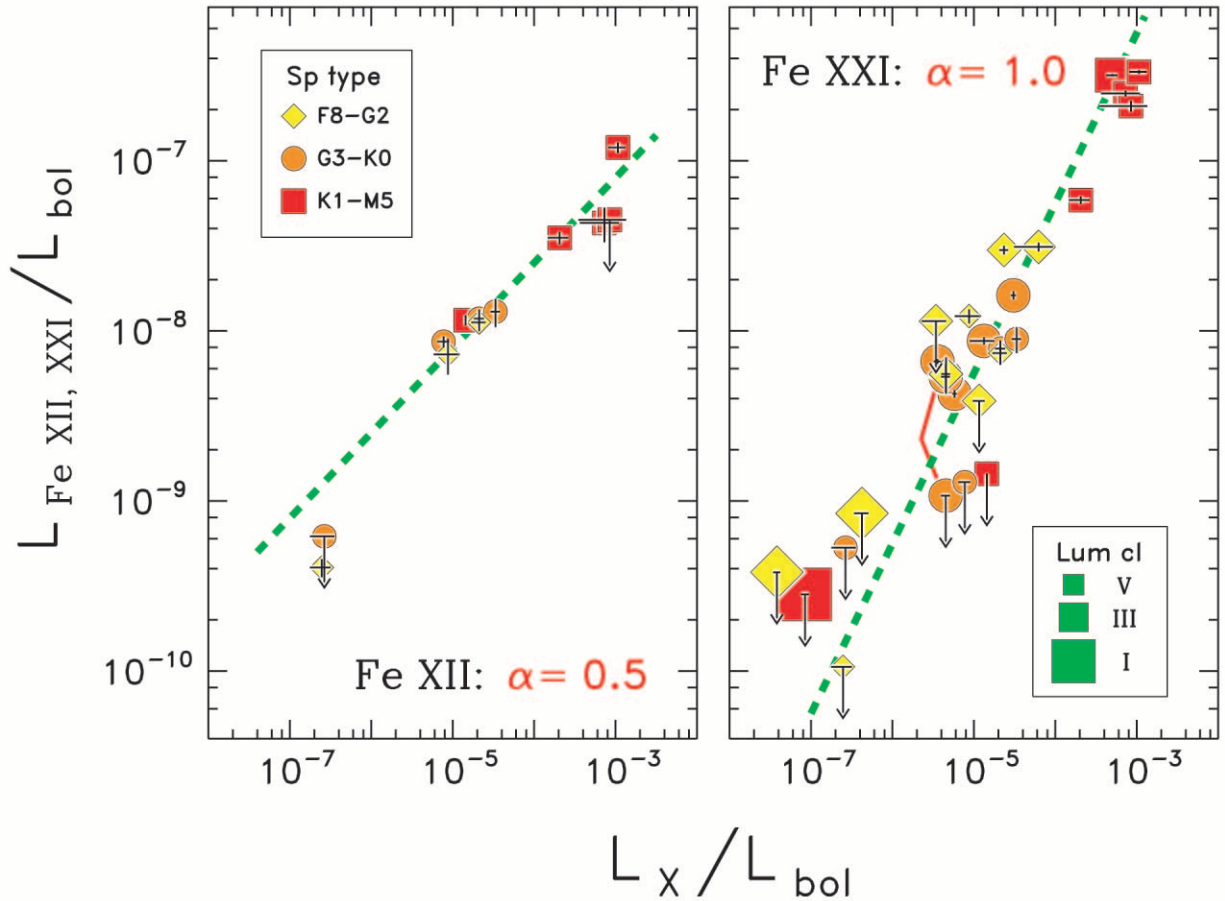


FIG. 7.—Comparison of normalized Fe XII (left) and Fe XXI (right) fluxes, and upper limits, with available *ROSAT* X-ray detections (0.2–2 keV). Different symbol sizes, shapes, and colors encode luminosity classes and spectral types according to the two legends. The dashed green lines are illustrative power laws adjusted to match the higher X-ray luminosity objects: $R_{Fe} \sim R_X^\alpha$. The kinked red line in the right-hand panel connects the GHRs detection of Fe XXI in the Capella G8 star with the 3σ upper limit from STIS.

(the true $v \sin i$ is 3 km s^{-1}) for the intrinsic line Doppler widths, which are controlled by thermal motions, large-scale flow fields, and turbulent motions in the stellar outer atmosphere. (Instrumental broadening can be ignored for the purposes here.) The remaining panels compare simple analytical rotational broadening models (Gray 1976) applied to the zero-rotation reference profiles. Here, in some cases, we subtracted an apparent low-amplitude “broad component” (see, e.g., Wood, Linsky, & Ayres 1998), modeling only the residual “narrow” core of the line. Such modifications are depicted as red dashed Gaussians in the upper traces of each split panel. In the case of Fe XXI, we also subtracted a model of the neighboring O I $\lambda 1355$ line because its blue wing interferes to some extent with the red wing of $\lambda 1354$, particularly in the fast-rotating stars. The resulting narrow-profile components are illustrated as circles and error bars on top of two rotational profiles (with different assumptions concerning the degree of limb darkening [narrower core] or brightening [flatter core], parameterized by Gray’s ϵ factor). The numerical entries in each panel indicate the $v \sin i$ that matches the empirical profile.

All three fast rotators show evidence that both the sub-coronal and coronal lines are broadened in excess of the photospheric $v \sin i$ (as estimated by the velocity appropriate for the chromospheric C I λ line). Redfield et al. (2003), in the companion *FUSE* study, found evidence for anomalously large broadening of the Fe XVIII $\lambda 974$

coronal forbidden line in the ultrafast rotating K dwarf AB Doradus (HD 36705; K1 V) and Hertzsprung gap giants 31 Com and Capella G1. Such “superrotational” broadening, if that is what causes the excess, could be a signature of highly extended coronal emission zones in these active stars, contrary to the very compact structures suggested by recent analyses of coronal densities and emission measures using line ratio diagnostics from *EUVE* (Dupree et al. 1993; Brickhouse & Dupree 1998) and, more recently, the *Chandra* transmission grating spectrometers (Brinkman et al. 2000). Extended coronal emission zones would, however, be expected in the “magnetospheric” scenario of Ayres et al. (1998), at least for the two Hertzsprung-gap giants. Ayres et al. viewed these “X-ray deficient” giants as transition coronal objects currently dominated by a fossil magnetosphere surviving from the main sequence (late-B or early-A) phase but beginning to develop a deep convection zone and a more solar-like regenerating magnetic dynamo.

5. CONCLUSIONS

We have surveyed an extensive sample of late-type stars, searching for UV coronal forbidden lines. Other than the Fe XII and Fe XXI features already identified in previous work, our search was largely negative. Nevertheless, we have demonstrated that the known coronal iron forbidden

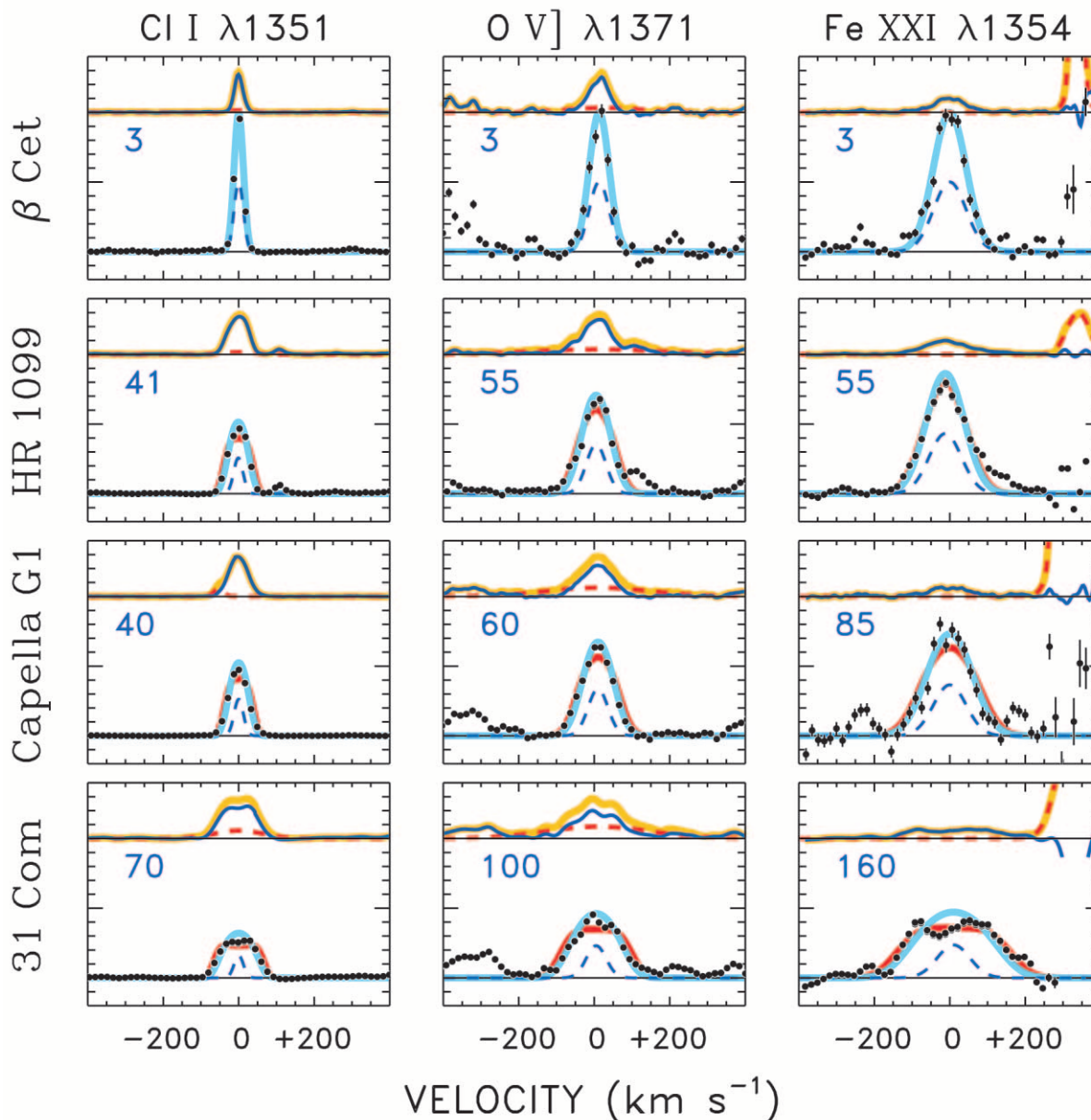


FIG. 8.—Comparison of chromospheric, subcoronal, and coronal line broadening in four stars. The upper entry, β Cet, serves as a low-rotation reference. Observed profiles are indicated by thick light orange curves in the upper part of each split panel. Various corrections for blends and/or “broad components” are depicted as red dashed curves, and the final profiles are shown as thin blue curves; these are repeated in the lower panel as black circles with $\pm 1 \sigma$ error bars and magnified as appropriate. The blue dashed curves show the “zero-rotation” reference profile (at half-scale), while the smooth curves under the observed line shape depict two spun-up versions of the reference, with different assumptions for the center-to-limb behavior (*red*: $\epsilon = -3$; *light blue*: $\epsilon = +1$ [in the notation of Gray 1976]).

lines occur in a wide range of active stars, at levels generally related to the *ROSAT* soft X-ray flux, although the power-law dependence is significantly flatter for Fe xxii compared with Fe xxii for X-ray indices above $R_X \sim 10^{-5}$.

As diagnostics of coronal flows and impulsive mass motions, the far-UV coronal forbidden lines have important advantages over X-ray permitted lines of, say, the Fe L-shell region near 1 keV: (1) the forbidden transitions are optically thin, even in dense flare plasmas; (2) UV instruments typically have a substantial advantage in spectral resolution over X-ray spectrometers; (3) the large effective area of UV normal incidence telescope optics compensates for the general faintness of the coronal forbidden lines; and (4) absolute velocity calibrations are routine in the UV, but not in soft X-rays.

We found that the Fe xxii $\lambda 1354$ feature, which is bright in active clump giants and dMe stars, is dominated by thermal broadening in most cases. We also found that Fe xxii normally does not exhibit a bulk redshift (or blue-shift), unlike subcoronal lines formed in the 5×10^4 – 2×10^5 K regime, which generally display systematic redshifts, perhaps symptomatic of downdrafts at the bases of coronal loops (Ayres et al. 1998). The general lack of bulk Doppler shifts in the Fe xxii features suggest that the hot, high emission measure zones in the stellar corona likely are trapped in confining structures, presumably analogous to solar magnetic loops. Any motions in such structures must be very subsonic and symmetrical (like a siphon flow). We certainly see no direct evidence for, say, a hot outflowing wind. (Such a wind might be present,

however, but its emission measure would have to be very small.)

Nevertheless, we do have one clear example of a Doppler shift in $\lambda 1354$, connected with the 1999 September multiwavelength campaign on HR 1099 mentioned in § 1. In the 7 hr period covered by STIS in that campaign, the Fe XXI feature steadily followed the orbital velocity of the K1 IV primary (the dominant coronal emitter in the HR 1099 system), although with a slowly increasing redshift, but departed briefly from the orbital track to exhibit a $\sim 20 \text{ km s}^{-1}$ blueshift at the peak of the first of two flares detected primarily in Si IV and C IV (Ayres et al. 2001). It will be important in the future to search for other examples of Fe XXI Doppler shifts in coronal outbursts as a crucial signature of the otherwise “hidden” dynamical side of the flare energy budget.

Among the faster rotating stars of our sample observed with reasonable S/N, there is evidence that Fe XXI $\lambda 1354$ is substantially broader than in the more slowly rotating objects. This could indicate highly extended coronal structures, such as inferred from the superrotational broadening of UV subcoronal emission profiles in Hertzsprung-gap giants (Ayres et al. 1998). The existence of highly extended coronal emission regions might conflict with studies of X-ray line ratios of helium-like triplet species and EUV density diagnostics, both of which argue for very high coronal pressures, implying compact emission volumes presumably

close to the star. The resolution of the dichotomy awaits future observations and modeling.

The potential value of the UV coronal iron forbidden lines for exploring coronal structure and dynamics in late-type active stars should be boosted significantly when the new generation Cosmic Origins Spectrograph (COS: Green 2001) is installed in *HST*. COS is a high-performance spectrometer with an order of magnitude more sensitivity than the corresponding grating modes of STIS and with sufficient resolution ($R \sim 2 \times 10^4$) to permit accurate deblending of $\lambda 1354$. COS will fuel a whole new range of coronal studies, serving as a bridge to that future era when X-ray spectroscopy matures into the high-resolution realm that has been the sole domain of ultraviolet space observatories for more than three decades.

This work was supported by grants GO-08280.01-97A from STScI and S-56500-D from NASA. Observations were from the NASA/ESA *HST*, collected at the STScI, operated by AURA, under contract NAS 5-26555. This research also made use of the SIMBAD database, operated by CDS, Strasbourg, France; the *ROSAT* X-ray archive at the HEASARC of the NASA Goddard Space Flight Center; and the Atomic Line List (<http://www.pa.uky.edu/~peter/atomic>). We thank the other collaborators in *HST* program 8280 for their help in carrying out the STIS stellar survey upon which the present work partly is based.

APPENDIX A

C I DEBLENDING STRATEGY FOR Fe XXI

In previous work on HR 1099 and Capella, the Fe XXI+C I blend typically was modeled as a sum of Gaussian profiles in which the width of the chromospheric component was set to a value deduced empirically from fits to less blended C I features in the vicinity. That approach was suited to the earlier GHRS spectral material, for which only a restricted wavelength interval normally was observed at one time ($\Delta\lambda \sim 35 \text{ \AA}$ for the G160M medium-resolution mode). However, the broad spectral grasp of STIS offers the possibility to explore other ways to correct for the C I blend. We developed the following strategy.

For each star, a surrogate profile of the C I feature was constructed by combining several clean low-excitation lines from the 1200–1700 \AA region. A list of target features was established for each star by interrogating a larger group of potential candidates using a semiautonomous line finding and fitting procedure, then selecting those that visually appeared to be free of close-in extraneous blends. In the case of Capella, we focused solely on C I lines owing to the depleted carbon abundance of the G8 star (a clump giant) relative, say, to oxygen; but for the other stars, we considered weak narrow features of a wide range of chemical species.

The selected profiles were individually normalized to their integrated fluxes in a velocity range restricted to the extreme line core, then compared with the other profiles on a common velocity scale. The high-fidelity wavelengths of the STIS echellograms, established by the onboard Pt-Ne lamp, ensured that the profiles were properly aligned to a small fraction of a pixel. The comparison procedure identified any intervals where a particular profile deviated significantly from the mean and omitted that portion of the line shape from a subsequent average. The result was a high signal-to-noise mean empirical profile representative of a typical optically thin low-excitation line. The method avoids measurement errors encountered in Gaussian modeling of individual weak lines and retains automatically any non-Gaussian aspects of the profile shapes, weak broad wings for example.

Having obtained a surrogate mean profile of C I $\lambda 1354.288$, the next step was to estimate the integrated flux to associate with the blend. Ideally, we would find another C I feature, somewhere else in the spectrum, whose intensity correlates well with that of $\lambda 1354.288$ but is not contaminated by extraneous blends. That feature then could serve as a proxy to establish the $\lambda 1354.288$ flux in each star. For example, C I $\lambda 1602$ ($2p^1S_0-4d^1P_1^o$) shares a common upper level with $\lambda 1354$ ($2p^1D_2-4d^1P_1^o$), and thus should be an accurate proxy, if both lines are optically thin. There are other transitions, such as $\lambda 1311$ ($2p^1D_2-5d^1F_3^o$), that arise from the same lower level as $\lambda 1354$ and thus should be reliable proxies if the C I lines are excited purely by collisions in a thermal environment that is similar in all of the stars. Unfortunately, the best candidate lines also tend to be very weak, like $\lambda 1354$ itself, thus allowing measurement error to compromise the value of the proxy. At the other extreme is the resonance multiplet of C I $\lambda 1657$ (UV 2), a collection of partially blended optically thick lines at the long-wavelength end of the STIS E140M band—a prominent spectral feature in late-type stars. Here one buys high accuracy in the flux measurement and relative freedom from extraneous blends at the expense of a possibly different excitation mechanism that might prevent a

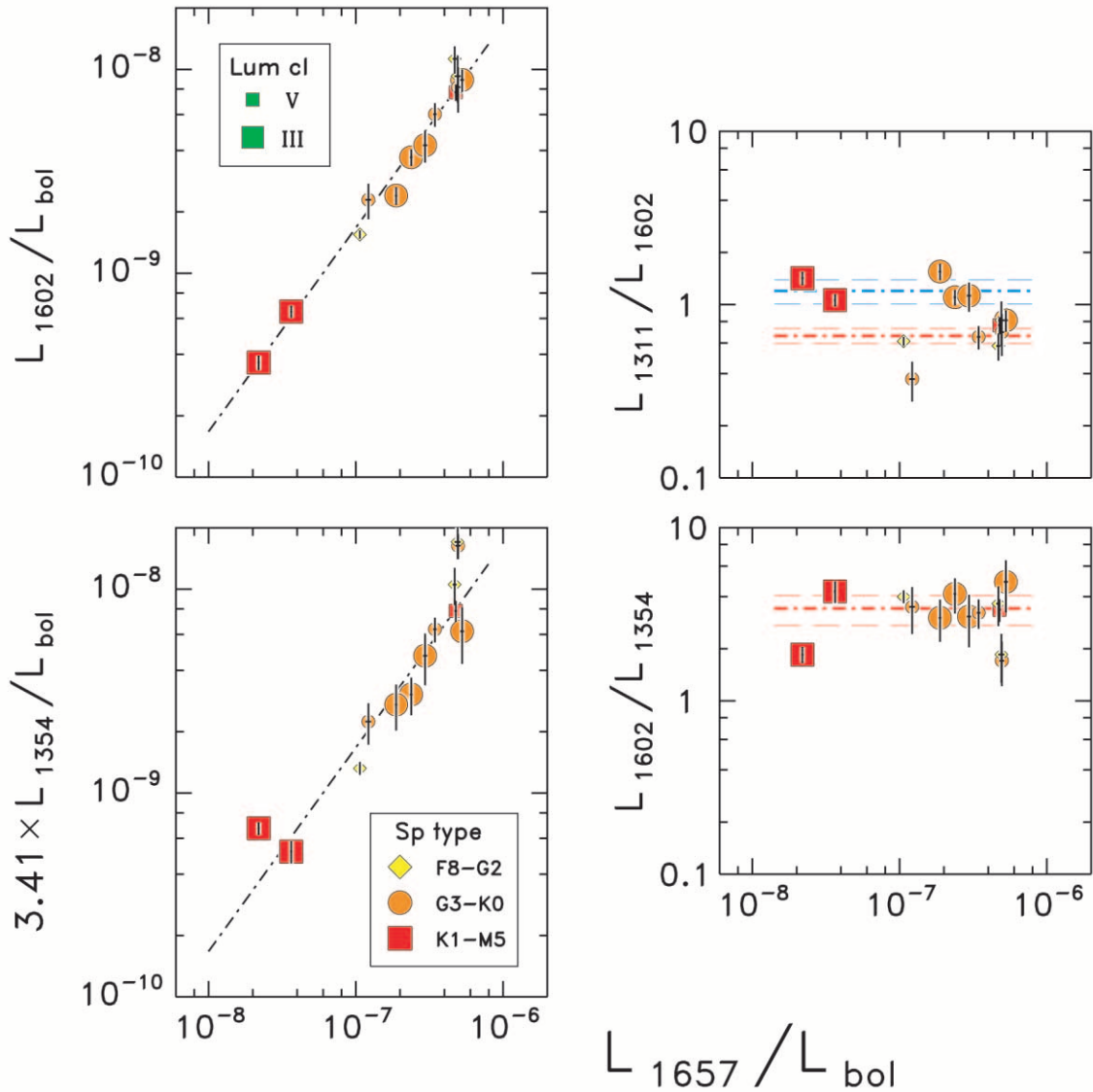


FIG. 9.—Correlation and ratio diagrams depicting trends of several key C I line intensities with respect to the strong $\lambda 1657$ multiplet. The objective was to develop a scaling law to predict the flux of C I $\lambda 1354$ so that it could be deblended from Fe xxI. The red square farthest to the left in each panel is the inactive red giant α Tau (K5 III).

seamless scaling to weak $\lambda 1354$. Fortunately, the several stars in the sample that are coronally inactive provide a baseline $\lambda 1354$ feature to test possible predictive scaling laws.

Figure 9 illustrates trends of several key C I line intensities and flux ratios with respect to strong $\lambda 1657$. In the lower right-hand panel, the ratio of $\lambda 1602$ to $\lambda 1354$ is depicted as a function of the $\lambda 1657$ activity “index” for the stars in which both features could be measured reliably. For the handful of low-activity stars clearly lacking Fe xxI, the $\lambda 1602/\lambda 1354$ ratio appears to be relatively independent of stellar type or luminosity class, except for “noncoronal” α Tau (*leftmost red square*), where C I $\lambda 1354$ itself is contaminated by another line, which we tentatively have attributed to Cr II. Two other (high-activity) stars also are discrepant in the 1602/1354 panel, but their C I fluxes were determined in an indirect “subtractive” procedure described below. C I $\lambda 1311$ is another possible proxy, but its ratio with $\lambda 1602$ (*upper right-hand panel*) displays systematic deviations that depend on luminosity class, and thus it proved unsatisfactory. We therefore adopted $\lambda 1602$ as a surrogate for $\lambda 1354$ to further investigate possible scaling laws (because we could measure $\lambda 1602$ in those stars in which C I $\lambda 1354$ itself was blended with a significant Fe xxI feature).

The upper left-hand panel depicts the empirical relationship between $\lambda 1602$ and the $\lambda 1657$ multiplet. The power-law slope is unity, showing that the subordinate and resonance line fluxes maintain a tight 1 : 1 correlation, without any dependence on surface temperature or gravity. Accordingly, we adopt the $\lambda 1602$ versus $\lambda 1657$ scale factor, multiplied by the empirical $\lambda 1354/\lambda 1602$ ratio in the low-activity objects, to convert the easily measured, blend-resistant $\lambda 1657$ flux to the equivalent C I $\lambda 1354$ strength: $f_{1354} \sim 4.9 \times 10^{-3} f_{1657}$.

Figure 10 is a montage of uncorrected Fe xxI features of nine stars ranging from G0 V to K0 III (the seven stars comprising the sample used for the mean coronal profile of Fig. 5 and two additional active G dwarfs). The dot-dashed curve in each profile represents the Gaussian model from Figure 5 adjusted in flux according to the blue side of the coronal forbidden line,

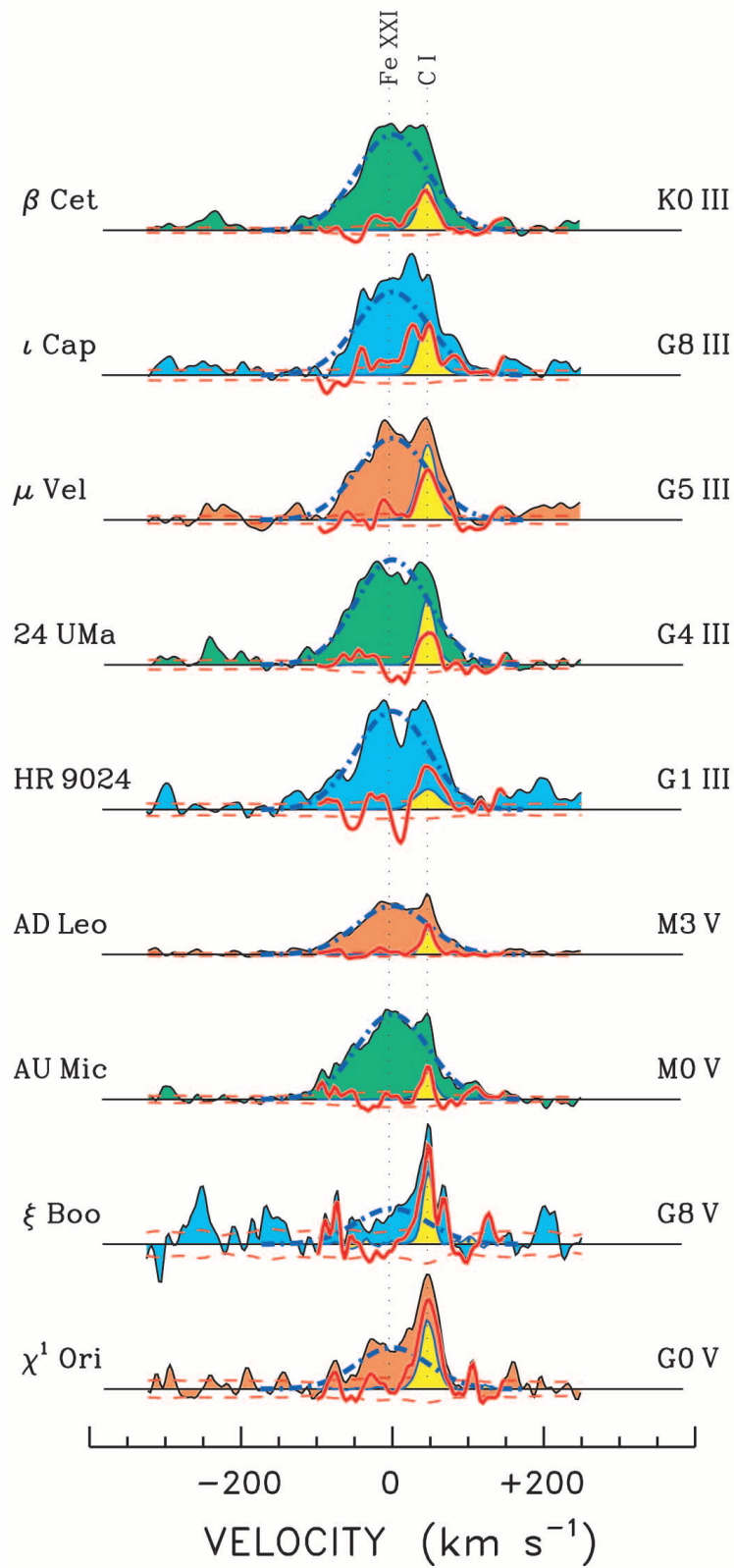


FIG. 10.—Montage of uncorrected Fe XXI features, with scaled mean profiles from Fig. 5 (blue dot-dashed curves). The red traces are the residuals after subtracting the model Fe XXI line shapes and should be compared to the narrow yellow profiles, which are the predicted C I $\lambda 1354$ features. The horizontal red dashed curves indicate $\pm 1 \sigma$ photometric uncertainty levels.

where the influence of the C I blend is minimal. The red curves are the result of subtracting the Gaussian model for Fe xxI and should be compared with the narrow yellow profiles, which are predicted C I $\lambda 1354$ features according to the $\lambda 1657$ scaling law. The agreement between the empirical residual profiles and the predicted C I blends generally is good, indicating that the deblending strategy works satisfactorily. The few significant deviations, 24 UMa for example, arguably could be attributed to local structure in the Fe xxI peak, which would cause the scaling procedure for the mean Fe xxI profile to overestimate the line strength and subtract too large a wing “background” from the vicinity of the C I blend. The horizontal red dashed curves indicate $\pm 1 \sigma$ photometric uncertainty levels, which include compensation for the Gaussian smoothing applied to the spectra. We measured the residual “C I” profiles in these subtractive examples and included the implied fluxes in the two lower panels of Figure 9 for comparison.

APPENDIX B

CORONAL VARIABILITY OF CAPELLA

B1. Fe xxI IN THE GHRS AND STIS EPOCHS

Johnson et al. (2002) recently described multiple Gaussian modeling of the STIS observation of Capella, concluding that the G8 III primary component—prominent in the GHRS spectrum analyzed by Linsky et al. (1998)—had faded into apparent invisibility. This was a somewhat ironic development, given that the previous detection of both stars of the binary at nearly equal coronal Fe xxI levels had been hailed as further confirmation of the unusual spectral properties of the X-ray-bright system. Despite complete dominance of UV emission lines in the temperature range 2×10^4 – 2×10^5 K by the G1 III star (Ayres & Linsky 1980), it nonetheless belongs to the class of “X-ray-deficient” Hertzsprung-gap giants identified by Simon & Drake (1989). Meanwhile, the G8 III star, which is relatively weak in the UV “hot” lines, nevertheless belongs to the class of active clump giants (β Cet [K0 III] is the prototype) that are bright coronal X-ray sources. Indeed, Ayres et al. (1983) anticipated this dichotomy after comparing spectrally separated UV emissions of the Capella giants with single stars of similar types. They concluded that the G8 star might contribute as much as half of the coronal soft X-ray flux of the system (which is not resolved spatially or spectrally in X-rays).

The GHRS dissection of Fe xxI into nearly equal contributions was seen as confirmation of that suggestion. Now, the new STIS observation seemingly implied that the primary had faded into Fe xxI obscurity, possibly indicating a much reduced coronal contribution to the overall soft X-ray flux of the system. On the other hand, since Fe xxI forms at higher temperatures than the $10^{6.8}$ K peak in Capella’s coronal emission measure distribution, perhaps the significant variability was confined primarily to the high-temperature tail (Johnson et al. 2002). Indeed, β Cet itself recently was shown to exhibit substantial variability between long *EUVE* pointings 6 yr apart (Ayres et al. 2001), with the most dramatic changes at the highest temperatures (represented, for example, by Fe xxIII $\lambda 133$).

Since Johnson et al. considered only the STIS Fe xxI profile, we felt it worthwhile to attempt a joint fit with the independent GHRS observation, in order to uncover, perhaps, a weak contribution from the G8 star during the STIS epoch, which might have been missed in those authors’ heavily constrained multiple Gaussian modeling. Furthermore, Johnson et al. neglected to consider other possible signatures of coronal activity in the STIS bandpass, He II $\lambda 1640$ B α for example.

Figure 11 presents a detailed view of the STIS and GHRS Fe xxI spectra of Capella. The circles are the individual observations, continuum-subtracted and corrected for the C I blend according to our empirical method. The GHRS spectrum was interpolated onto the STIS wavelength scale and accurately registered by cross-correlation of a ~ 10 Å swath in common to the two observations. Both spectra then were smoothed with a 4 pixel Gaussian. The STIS resolution is twice that of GHRS, although the difference is not especially important for the highly broadened Fe xxI feature. The effect is visible, however, in the O I $\lambda 1355$ wing, at $+200$ km s $^{-1}$. The velocity scale is in the reference frame of the G1 star. The zero point was established empirically by the average of a sample of chromospheric emission lines for which the (dominant) G1 component could be measured with minimal contamination by the G8 star.

The orange and yellow shaded profiles in the lower panel indicate the inferred contributions of the G8 and G1 stars, respectively, to the GHRS spectrum. The blue curve is the total, including instrumental and Gaussian smoothing. These are the optimum models obtained after an extensive investigation of the parameter space (allowing, for example, one or both Fe xxI profiles to deviate from the stellar rest frame). The FWHM and Doppler shift was assumed the same for a given star in both the STIS and GHRS fits, but differences *between* the stars were allowed. Any G8 “shift” is relative to the expected 53 km s $^{-1}$ orbital velocity difference between the two stars at $\phi = 0.73$. The best fit was $\Delta v = 0$ km s $^{-1}$ for both stars: in other words, all the Fe xxI profiles are at rest with respect to the predicted orbital velocities.

These fits support the conclusion by Johnson et al. (2002) that the Fe xxI flux of the G8 star was severely reduced during the STIS epoch. However, those authors assumed identical FWHMs for the two stars, 108 km s $^{-1}$. We find about the same width in the optimum fit for the G8 star (104 km s $^{-1}$) but a significantly broader contribution for the G1 star. If we derive a mean Fe xxI profile like that of Figure 5, but solely for the late-type active giants, we obtain FWHM ~ 106 km s $^{-1}$, in agreement with both analyses for the G8 star. The advantages to our method for isolating the Fe xxI components are (1) that empirically subtracting the C I profile avoids having to introduce the additional Gaussian components in an already only lightly constrained problem and (2) that exploiting the two epochs provides additional information, particularly concerning the width of the G1 profile. (The issue of the line shape of the G1 star is discussed in § 4.2, concerning coronal forbidden line widths in fast-rotating stars.)

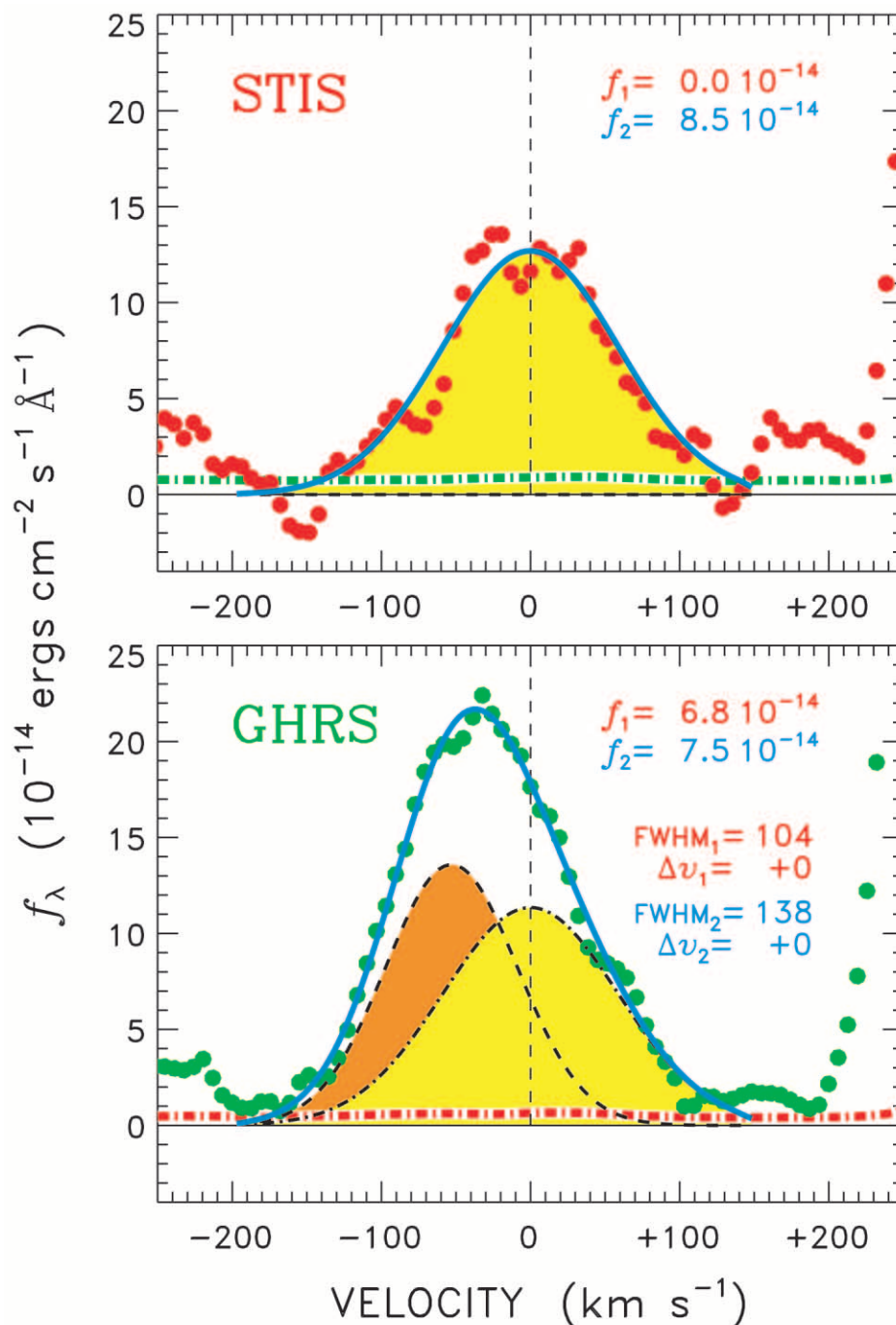


FIG. 11.—Gaussian modeling of GHRs (*bottom*) and STIS (*top*) spectra of Capella in the region of Fe xxI. The circles are the individual observations, continuum-subtracted and corrected for the C I blend. The horizontal dot-dashed curves indicate 1σ photometric uncertainty levels. The velocity scale is in the reference frame of the G1 star, as established empirically. The orange and yellow shaded line shapes in lower panel indicate inferred contributions of the G8 and G1 stars, respectively, modeled as single Gaussian profiles. The blue curve is the composite line shape, including instrumental broadening (STIS resolution is twice that of GHRs). For the tabulated Gaussian parameters (integrated flux f , FWHM, and Δv), the subscripts 1 and 2 refer to the G8 (primary) and G1 (secondary) stars, respectively.

B2. THE He II BALMER α EMISSION

We now turn our attention to the He II B α line, which is thought to be at least partially formed by a photoionization/recombination process driven by coronal EUV radiation fields (in the He II continuum shortward of 228 \AA ; see, e.g., Linsky et al. 1998 and references to previous work therein). Thus, the He II flux potentially can serve as a proxy for the intensity of the EUV radiation fields, which are dominated by coronal iron lines (see Dupree et al. 1993).

The He II $\lambda 1640$ interval was observed during the same GHRs program in 1995 that obtained the Fe xxI spectrum (at orbital phase 0.73). After correcting for the slight difference in flux scales described in § 2.3, the GHRs and STIS spectra are nearly identical, aside from a small deviation in the blue side of the STIS He II line core at the expected radial velocity of the G8 star.

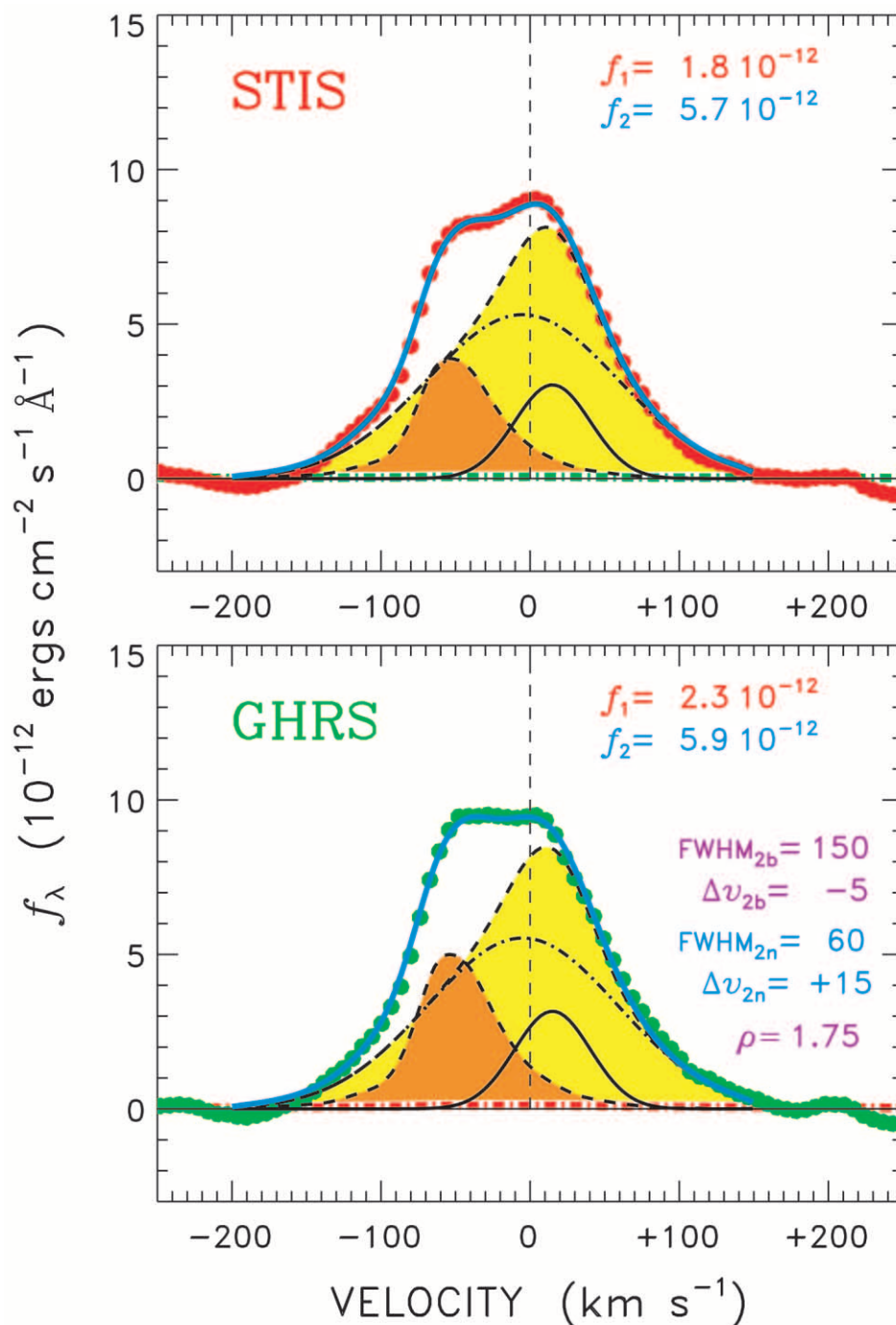


FIG. 12.—Analogous to Fig. 11, but for He II $\lambda 1640$. The red and green circles are the observed profiles, continuum-subtracted and corrected for the O I $\lambda 1641$ blend. The G8 star is represented by an empirical line shape (orange shaded) derived from single clump giants of similar activity level. The G1 star (yellow shaded) is modeled as the sum of a dominant broad component (dot-dashed curves) and a subordinate narrow component (solid curves); ρ is the ratio of the broad/narrow peak fluxes. The sum of the G8 and G1 contributions, including the respective instrumental broadenings, is the blue solid curve.

Figure 12 is analogous to Figure 11, showing our optimum joint fit to the GHRS and STIS epoch profiles. We subtracted a continuum level and compensated for the O I $\lambda 1641$ blend in the red wing of He II, using a correction strategy similar to that applied to the C I blend in Fe XXI. Examination of the He II profiles of slowly rotating active G/K giants in the sample (24 UMa, μ Vel, ι Cap, and β Cet) showed that they all were nearly identical in shape but clearly non-Gaussian, with a dominant narrow core on top of a broader, redshifted base. We constructed an empirical mean He II profile, in the same way as for Fe XXI in Figure 5, and utilized it directly in the least-squares modeling to represent the G8 component. Again, the advantage here over conventional multi-Gaussian modeling is the use of empirical information to constrain as much of the problem as possible.

Unfortunately, lacking an empirical estimate of the He II profile of the G1 star, we were forced to model it as a pair of Gaussians: one broad, the other narrow. Our motivation was partly from the earlier work of Linsky et al. (1998), who described the different broadening of components of the He II line expected for (1) direct collisional excitation in a hot subcoronal plasma and (2) photoionization/recombination in lower lying cooler regions. Additional motivation for the double-Gaussian fit was the example of the average clump giant profile. The best combination we found for the G1 star was a broad, slightly blueshifted, main component and a narrower slightly redshifted subsidiary component. The overall asymmetry is opposite to that of the G8 star (whose narrow component is slightly blueshifted relative to the broad base). The significance of the opposite asymmetries remains to be clarified. It is also not clear whether the broad and narrow components in the G8 and G1 profiles should be interpreted in terms of the formation mechanisms described by Linsky et al. or whether they are the result of the same dynamical processes that cause broad and narrow components in other hot lines like C IV λ 1548, where only collisional excitation is important. Aside from that uncertainty, the outcome of the modeling is that the G1 component of He II appears not to have changed between the two epochs, whereas the G8 component displayed about a 20% drop in the more recent spectrum.

The apparent change in the He II flux of the G8 star is not unprecedented. In fact, Linsky et al. called attention to a nearly identical deficit between the $\phi = 0.73$ GHRS G160M He II profile in 1995 and one obtained 7 months (two binary orbits) later in 1996 using GHRS ECH-A at $\phi = 0.78$, when the G8 and G1 stars have the same radial velocities as at $\phi = 0.73$. The authors found about the same 20% decline in the G8 contribution to the composite He II line. They attributed the decline to a reduction in the EUV photoionizing flux levels of the G8 star, appealing to changes of similar magnitude documented in (non-contemporaneous) *EUVE* spectra of the binary (see Dupree et al. 1999).

The important conclusion of the present analysis is that the G8 star varied much less in He II than in Fe XXI, supporting the idea that the dominant change was to the high-temperature tail of the emission measure distribution of the G8 star rather than a bulk depression of its entire coronal emission. An analogous effect is seen in the solar corona over the sunspot cycle: hot active regions dominate at the peak, but the cooler background structures of the quiet corona dominate during minimum.

APPENDIX C

ROSAT SOFT X-RAY FLUXES

We conducted a careful evaluation of soft X-ray fluxes from the *ROSAT* archive for the sample stars. Most of the targets were detected in the *ROSAT* All-Sky Survey (RASS), and many have individual pointings using the Position Sensitive Proportional Counter (PSPC), boron-filtered PSPC (which suppresses the soft part of the spectrum below 0.3 keV), or the High-Resolution Imager (HRI) (see Pfeiffermann et al. [1987] for a description of these instruments and observing modes).

There are several catalogs that summarize stellar X-ray fluxes based on the *ROSAT* survey phase (the RASS Bright Source Survey [RASSBSC]) or on pointed material, such as the so-called WGACAT (a private effort of N. E. White, P. Giommi, & L. Angelini²) and the “official” databases ROSPSPC and ROSHRI developed by the participating *ROSAT* institutions. These catalogs have the advantage of covering broad classes of objects in a more or less homogeneous way, but they have certain disadvantages. First, the catalogs report count rates in different “standard” bandpasses (e.g., 0.24–2.0 keV for WGACAT but 0.1–2.4 keV for ROSPSPC and RASSBSC) and utilize different methods to find and measure the significant sources. Thus, intercomparisons are not straightforward. The existing catalogs also do not include the “filtered” PSPC observations, which comprise 25% of the PSPC data sets we examined. In some cases, such as the α Centauri system ($\Delta r \sim 20''$), the stellar sources are partially resolved at HRI resolution (FWHM $\sim 7''$), in principle providing additional information than is available in the standardized extraction. Furthermore—especially for off-axis sources in serendipitous fields—one must treat the cataloged count rates with caution if the vignetting is large, or the source falls partially behind the window support structure of the PSPC. Most importantly, stellar coronal sources, particularly the “active” ones, tend to be variable on a broad range of timescales, so it is important to be able to combine measurements from the different instrument modes to evaluate such variability, if possible.

We therefore remeasured all of the pointed observations in the *ROSAT* archive for the target stars, using custom PSPC software described by Ayres et al. (1998), modified for the present study and extended to the HRI. In all, we analyzed nearly 50 PSPC and 75 HRI observations (about 50 of the latter were of the α Cen system). We examined calibration observations primarily of the RS CVn binary AR Lac and the bright BL Lac object Mrk 421 to determine the spatial point response functions for the HRI and the PSPC (the latter exhibits a strong energy dependence on-axis). The optimum detect circle radius r is determined, in principle, by the trade-off between the growing encircled energy as r increases and the larger background (noise) from the enlarging source area. Beyond a critical radius r_{crit} , the background noise contribution increases faster than the source signal from the increment in encircled energy and the S/N of the source detection begins to decline. For a relatively weak, background-dominated source, and a nearly Gaussian point-spread function (PSF) such as that of the PSPC, the break-even point falls near the 85% encircled energy radius ($\sim 30''$). However, for the PSPC, the PSFs are strongly energy dependent, and using the “optimum” r for 0.24–2 keV photons could compromise the collection of the softer 0.1–0.24 counts (which are utilized in a “hardness ratio” to estimate appropriate energy conversion factors [ECF]). We therefore adopted a more conservative $r = 75''$ detect radius for the PSPC, which includes greater than 97% of the 0.24–2 keV photons and $\sim 90\%$

² See N. E. White, P. Giommi, & L. Angelini (2000), WGACAT version of the *ROSAT* PSPC Catalogue, Rev. 1, Laboratory for High-Energy Astrophysics (LHEA/NASA), Greenbelt, at <http://wgacat.gsfc.nasa.gov/wgacat/wgacat.html>.

of the 0.1–0.24 photons. The HRI PSF has a narrow core but broad scattering wings, and it was necessary to use $r = 25''$ (about 3 times the inferred r_{crit}), corresponding to the 90% encircled energy radius. This accommodates the range of encircled energy functions derived from Mrk 421 and a variety of bright cool-star sources of different coronal temperatures. For off-axis sources in PSPC fields, we boosted the detect radius appropriately (based on PSPC observations of Capella, $\sim 40'$ from field center) to compensate for vignetting.

Source strengths were measured as follows: Initial source counts were collected from the event list in a $2'$ diameter circle (PSPC) centered on the predicted coordinates of the target in the X-ray image. If there was sufficient source contrast, the centroid was adopted; otherwise the original predicted position was used. A background count rate per square arcminute was determined by dividing a $10' \times 10'$ area around the source circle into $32 \ 100'' \times 100''$ cells, excluding the $200'' \times 200''$ inner box surrounding the source, and discarding those cells in the lower and upper parts of the count distribution, to account for low-sensitivity areas (shadows of the window support mesh) and discrete sources, respectively. The average background, restricted to the pulse height channels corresponding to a specific energy range (say, 0.24–2 keV), was scaled to the source extraction area and subtracted. The net counts then were divided by a factor to account for the encircled energy radius and by an integration time extracted from the “exposure map” (which compensates for the blurring of low-sensitivity areas by the dither pattern). We determined a “hardness ratio” $(A - B)/(A + B)$, where A is the count rate in the 0.5–2.0 keV “hard” band and B is that in the 0.1–0.4 keV “soft” band, by repeating the process for the counts selected from the appropriate pulse-height intervals. Upper limits ($N_{3\sigma}$ in counts) were derived from the average background N_B in the detect cell according to $N_{3\sigma} \sim 3(N_B)^{1/2} + 1.6$, as inferred from Monte Carlo simulations of the Poisson detection process.

We used the WebPIMMS exposure time simulator (courtesy of the High-Energy Archive Science and Research Center [HEASARC]) with a variety of Raymond-Smith thermal models to estimate ECFs (in units of 10^{-12} ergs cm^{-2} count^{-1} at Earth in the reference energy band 0.2–2 keV) for the PSPC and HRI. Converting from the full PSPC band (0.1–2.4 keV), we found ECF ~ 3 for the softest sources (HR < -0.85) and 7 for the harder ones; for the more restricted standard band of the WGACAT and our reductions (0.24–2 keV), ECF ~ 10 , relatively independent of hardness. Converting from the HRI band (0.1–2 keV), we find ECF ~ 25 , again relatively independent of HR over the range typical of coronal sources. We also derived a count ratio of unfiltered/filtered PSPC of 2.5 ± 0.1 by comparing appropriate data sets for five of our targets, leading to ECF ~ 25 for filtered PSPC observations.

For α Cen A (G2 V), which is partially resolved from its companion (α Cen B [K1 V]) in the HRI but not in the PSPC, we relied mainly on the large collection (nearly 50) of HRI exposures, measuring the partially blended double image with a modified version of our standard event list procedure. The G-type component showed relatively little variability over the 1995 June–1998 January period, while the K-type companion on average was slightly more than twice as bright (in HRI counts). The secondary also displayed short-term, systematic changes in its X-ray luminosity reminiscent of rotational modulations (particularly in the second half of 1996), at least one significant flare, and perhaps a long-term decline like that expected from a magnetic cycle.

We then considered the individual measurements for each star of the full sample, consisting of the RASSBSC flux and any additional pointings, all converted to fluxes at Earth in the reference 0.2–2 keV band. We discarded the highest value of each set (flare filter), then combined the measurements without regard to exposure time, treating each as an independent sample. The resulting averages and our best estimates of the appropriate ranges are summarized in Table 3. It is important to emphasize that most of the X-ray detections are isolated snapshots of the stellar X-ray flux history and that the true coronal flux level during, say, the STIS measurements could have been quite different. Nevertheless, the *ROSAT* fluxes do represent the only large consistent database with which to assess the stellar coronal X-ray properties of our sample.

REFERENCES

- Allred, J. C., Hawley, S. L., Johns-Krull, C. M., & Fisher, G. H. 2002, *BAAS*, 34, 771
- Ayres, T. R., Brown, A., Osten, R. A., Huenemoerder, D. P., Drake, J. J., Brickhouse, N. S., & Linsky, J. L. 2001, *ApJ*, 549, 554
- Ayres, T. R., & Linsky, J. L. 1980, *ApJ*, 241, 279
- Ayres, T. R., Osten, R. A., & Brown, A. 2001, *ApJ*, 562, L83
- Ayres, T. R., Schiffer, F. H., III, & Linsky, J. L. 1983, *ApJ*, 272, 223
- Ayres, T. R., Simon, T., Stern, R. A., Drake, S. A., Wood, B. E., & Brown, A. 1998, *ApJ*, 496, 428
- Bennett, J. O., & Ayres, T. R. 1988, *PASP*, 100, 1129
- Brickhouse, N., & Dupree, A. K. 1998, *ApJ*, 502, 918
- Brinkman, A. C., et al. 2000, *ApJ*, 530, L111
- Day, R. W., Lambert, D. L., & Sneden, C. 1973, *ApJ*, 185, 213
- Dere, K. P., Bartoe, J.-D. F., & Brueckner, G. E. 1989, *Sol. Phys.*, 123, 41
- Doschek, G. A., et al. 1975, *ApJ*, 196, L83
- Dupree, A. K., Brickhouse, N. S., Doschek, G. A., Green, J. C., & Raymond, J. C. 1993, *ApJ*, 418, L41
- Dupree, A. K., Brickhouse, N. S., & Hanson, G. J. 1996, in *IAU Colloq. 152, Astrophysics in the Extreme Ultraviolet*, ed. S. Bowyer & R. F. Malina (Dordrecht: Kluwer), 141
- Dupree, A. K., Brickhouse, N. S., & Sanz-Forcada, J. 1999, *BAAS*, 31, 1483
- Edlén, B. 1945, *MNRAS*, 105, 323
- Feldman, U., Behring, W. E., Curdt, W., Schuehle, U., Wilhelm, K., Lemaire, P., & Moran, T. M. 1997, *ApJS*, 113, 195
- Feldman, U., Curdt, W., Landi, E., & Wilhelm, K. 2000, *ApJ*, 544, 508
- Feldman, U., & Laming, J. M. 2000, *Phys. Scr.*, 61, 222
- Gray, D. F. 1976, *The Observation and Analysis of Stellar Photospheres* (New York: Wiley), 398
- Green, J. C. 2001, *Proc. SPIE*, 4498, 229
- Güdel, M., Guinan, E. F., & Skinner, S. L. 1997, *ApJ*, 483, 947 (GGS)
- Hartmann, L., Dupree, A. K., & Raymond, J. C. 1980, *ApJ*, 236, L143
- Johnson, O., et al. 2002, *ApJ*, 565, L97
- Jordan, C., McMurry, A. D., Sim, S. A., & Arulvel, M. 2001, *MNRAS*, 322, L5
- Lindler, D. 1999, *STIS-IDT CALSTIS Manual* (version 1999 April; Greenbelt: NASA/LASP)
- Linsky, J. L., & Haisch, B. M. 1979, *ApJ*, 229, L27
- Linsky, J. L., Wood, B. E., Brown, A., & Osten, R. A. 1998, *ApJ*, 492, 767
- Maran, S. P., et al. 1994, *ApJ*, 421, 800
- Mason, H. E., Shine, R. A., Gurman, J. B., & Harrison, R. A. 1986, *ApJ*, 309, 435
- Pfeffermann, E., et al. 1987, *Proc. SPIE*, 733, 519
- Redfield, S., Ayres, T. R., Linsky, J. L., Ake, T. B., Dupree, A. K., Robinson, R. D., & Young, P. R. 2003, *ApJ*, in press
- Robinson, R. D., Airapetian, V. S., Maran, S. P., & Carpenter, K. G. 1996, *ApJ*, 469, 872
- Sandlin, G. D., Brueckner, G. E., & Tousey, R. 1977, *ApJ*, 214, 898
- Schmitt, J. H. M. M., & Wichmann, R. 2001, *Nature*, 412, 508
- Shine, R. A. 1983, *ApJ*, 266, 882
- Simon, T., & Drake, S. A. 1989, *ApJ*, 346, 303
- Wood, B. E., Linsky, J. L., & Ayres, T. R. 1997, *ApJ*, 478, 745
- Woodgate, B. E., et al. 1998, *PASP*, 110, 1183
- Young, P. R., et al. 2001, *ApJ*, 555, L121